Article

Two-Stage Superimposed Gold Mineralization in the Xiejiagou Gold Deposit, Shandong Province: Insights from Fluid Inclusions, H-O-S Isotopes, and Trace Elements

Ze-Zhong Du [1,2], Zhi-Zhong Cheng [1,2,*], Xiao-Feng Yao [1,3] and Xing-Long Bao [4]

[1] Development and Research Center, China Geological Survey, Beijing 100037, China; dzezhong@mail.cgs.gov.cn (Z.-Z.D.); yxiaofeng@mail.cgs.gov.cn (X.-F.Y.)
[2] Technical Guidance Center for Mineral Exploration, Ministry of Natural Resources of China, Beijing 100037, China
[3] College of Earth Sciences, Chengdu University of Technology, Chengdu 610059, China
[4] Zhenghe Yuanxin Mining Corporation Limited, Nanping 353600, China
[*] Correspondence: czhizhong@mail.cgs.gov.cn

Abstract: The Xiejiagou gold deposit located in the Zhaoyuan-Laizhou gold belt is composed of altered-rock-type gold mineralization and superposed auriferous quartz veins, showing unique two-stage gold mineralization. Oxygen and hydrogen isotopic analyses yielded the following results: $\delta^{18}O_{H2O} = 0.8‰$ to $4.4‰$ and $\delta D = -106‰$ to $-85‰$ for altered-rock-type mineralization, and $\delta^{18}O_{H2O} = 3.6‰$ to $5.6‰$ and $\delta D = -98‰$ to $-89‰$ for auriferous quartz-veins. Combined studies on Co/Ni, Sb/Bi and As/Ag ratios of pyrites, it can be inferred that the ore-forming fluids were dominated by magmatic water mixed with very little meteoric water. The fractured altered rocks in the ore-hosting fault zones are characterized by mylonitization, cataclastic lithification, and structural lenses, reflecting a compressional (closed) ore-forming system. In contrast, the occurrence of auriferous quartz veins in fissures of altered-rock-type orebodies and the fact that altered-rock-type ores commonly occur as breccias cemented by auriferous quartz veins that reflect an extensional (open) ore-forming system for the vein mineralization. The increase in $\delta^{34}S$ values from stage I ($5.8‰–7.2‰$) to stage II ($6.6‰–9.0‰$) indicate that the altered-rock-type mineralization was the result of intense water–rock interaction, while the occurrence of immiscible inclusions in auriferous quartz veins demonstrates that fluid immiscibility contributes significantly to gold deposition in the vein-type mineralization. Fluid-inclusion microthermometric data indicate that the fluids for the altered-rock-type mineralization are characterized by moderate-to-high temperature (262–368 °C), and low-to-moderate salinity (4.3–10.8 wt.% NaCl equivalent). In contrast, halite-bearing inclusions are found in auriferous quartz veins, and its fluids are characterized by moderate-to-high temperature (290–376 °C) and moderate-to-high salinity (5.1–41.9 wt.% NaCl equivalent). From early stages (I and II) to the late stage (III), homogenization temperature and high temperature element (W, Sn, and Mo) concentrations in pyrite first decrease and then increase, $\delta^{34}S$ values and metallization-related element (Au, Ag, and Bi) concentrations in pyrite first increase and then decrease. Therefore, it can be inferred that the two distinct types of gold mineralization in the Xiejiagou gold deposit may be two separate mineralization events. The presence of magnetite in the auriferous veins suggests an increase in oxidation state during the vein mineralization. Importantly, the Xiejiagou gold deposit preserves two types of mineralization in a single deposit and uniquely records a metallogenic transition from a compressional, reduced environment to an extensional, oxidized environment, as a result of a regional stress field transition that occurred in the Zhaoyuan-Laizhou gold belt at ca. 120 Ma.

Keywords: fluid inclusions; H-O-S isotopes; auriferous quartz veins; metallogenic environment; regional tectonic shift; Xiejiagou gold deposit

1. Introduction

Since 2011, major achievements have been made in ore prospecting in the deep part of the Jiaodong Peninsula in eastern China. Among them are the discovery and evaluation of about 2958 tons of newly increased gold resources and 12 large gold deposits, as well as the discovery of two super-giant gold deposits [1]. The Jiaodong Peninsula has cumulative-proven gold resources of up to more than 5000 tons [2,3], accounting for one-third of China's gold reserves [1]. Gold deposits are typically controlled by NE- and NNE-trending faults and can be divided into the Linglong type and Jiaojia type [4]. The gold deposits of the Linglong type (also known as the auriferous quartz-vein type) are characterized by abundant auriferous quartz veins hosted in subsidiary second- or third-order faults with narrow alteration halos, while the gold deposits of the Jiaojia type (also known as the altered-rock type) consist of disseminated and stockwork ores and occur in regional faults with broad alteration halos (e.g., [5–7]). The western Jiaodong gold province is dominated by altered-rock-type gold deposits, while the eastern Jiaodong gold province mainly comprises the auriferous quartz-vein-type gold deposits. Recent exploration in the Jiaodong gold province has shown that many gold deposits contain both altered-rock and auriferous quartz-vein-type mineralization. The gold mineralization occurs in two patterns: (1) In the Jiaojia, Taishang, Luoshan, and Fushan gold deposits of the Zhaoyuan-Laizhou gold belt, quartz-vein-type ores occur commonly at depth, while shallow parts of the deposits are dominated by altered-rock-type ores [8,9]. (2) In the Hushan gold deposit of the Penglai-Qixia gold belt, gold mineralization is characterized by an early-stage altered-rock-type ore superimposed by a late-stage auriferous quartz-vein ore [6]. The Hushan gold deposit is located in the Taiqian-Douya Fault zone which seems to act as the boundary between the western altered-rock-type gold deposits and the eastern quartz-vein-type gold deposits in the Jiaodong gold province (Figure 1). Does the two-stage superimposed gold mineralization occur only in the Hushan gold deposit, which was formed in a somewhat special geological background? Is there any special relationship between the two-stage gold mineralization and the regional tectonic evolution? These questions are worth investigating.

Unlike most other gold deposits in the Zhaoyuan-Laizhou gold belt, which host only a single mineralization type, the Xiejiagou gold deposit in this belt has two distinct gold mineralization types, i.e., an early-stage altered-rock type (Jiaojia type) and a late-stage, superimposed auriferous quartz-vein type (Linglong type). Previous studies on the Xiejiagou gold deposit have shown that (1) the primary ore-forming fluids were of magmatic origin, and meteoric water was involved in the later metallogenic stage [10,11]; (2) gold was precipitated as the result of fluid cooling, fluid immiscibility, and/or decrease in f_{S2} [10–12]; and (3) gold mineralization occurred at 122–118 Ma during the Early Cretaceous [11]. However, the above-mentioned studies ignored the differences in the ore-forming environment and process between the two distinct mineralization types. This paper presents new results of a comprehensive study involving ore geology, fluid-inclusion microthermometry, H-O-S isotopes, and trace elements in pyrite from the Xiejiagou gold deposit. The major purpose is to examine the difference in geological and geochemical characteristics of the two types of gold mineralization at Xiejiagou and to provide new insights into the relationship between the two-stage gold mineralization and the regional tectonic evolution in the Zhaoyuan-Laizhou gold belt of the Jiaodong gold province.
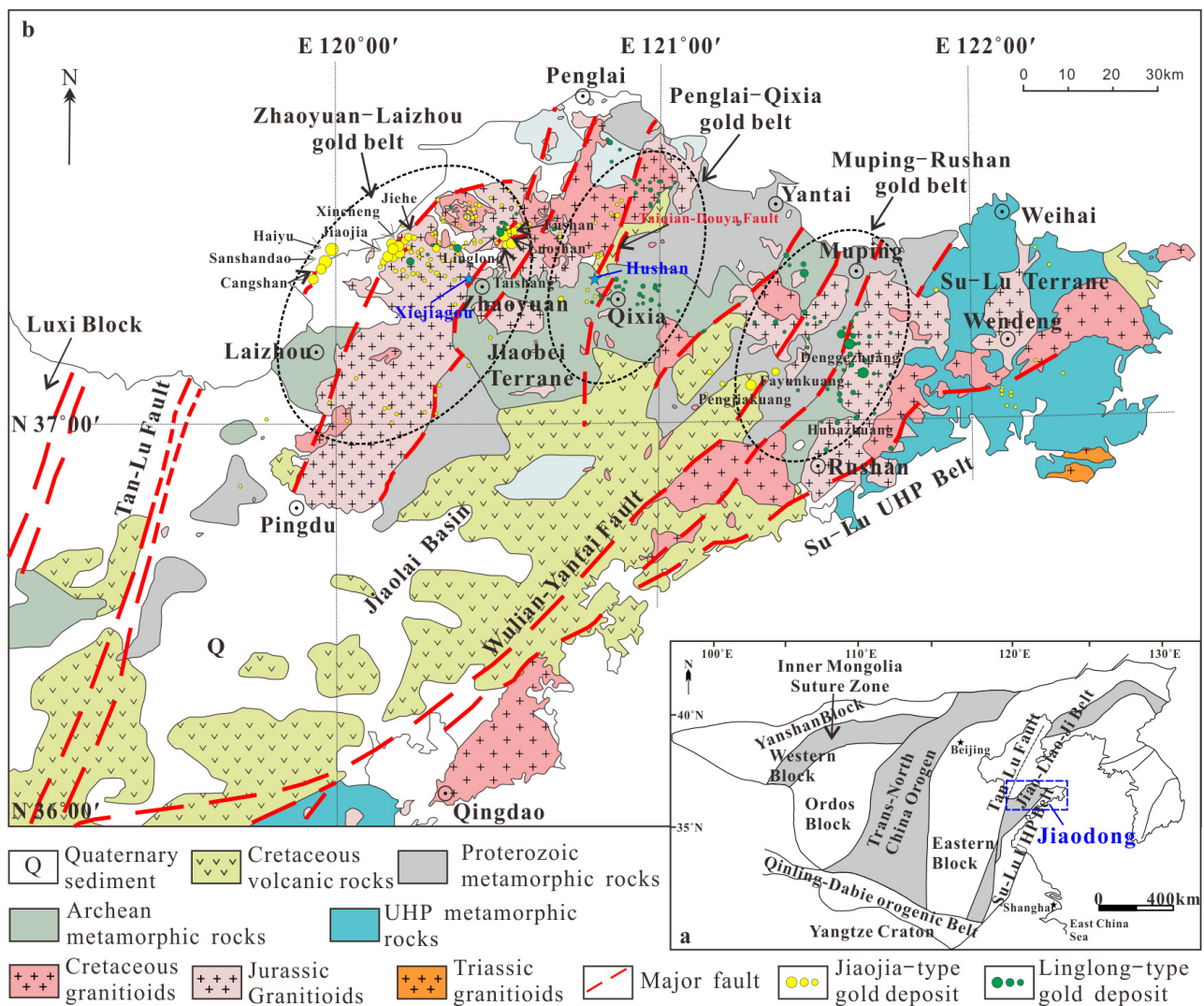
Figure 1. Simplified tectonic framework of the North China block (**a**) and geological map of the Jiaodong area (**b**) (modified after [13,14]).

2. Geological Background

The Jiaodong gold province is located in the eastern part of the North China block (Figure 1a) and is bounded on the west by the NE- to NNE-trending Tan-Lu fault zone and on the south by the Su-Lu ultrahigh-pressure metamorphic belt (Figure 1b). Exposed rocks in the area consist of metamorphosed Precambrian basement sequences and a series of Mesozoic intrusive and volcanic rocks [15]. The Precambrian sequences contain the Archean Jiaodong Group and the Proterozoic Jingshan and Fenzishan Groups, which are made up of mafic to felsic volcanic and sedimentary rocks metamorphosed to amphibolite and granulite facies [16,17]. The Mesozoic volcanic rocks, specifically the Lower Cretaceous Qingshan Formation, are mainly distributed in the Jiaolai Basin, and were formed between 108 and 110 Ma [18]. The Qingshan Formation comprises two units, with the lower assemblage composed of trachybasalt, latite, and trachyte, overlain by an upper assemblage dominated by rhyolite flows and pyroclastic rocks [5,19].

Mesozoic intrusions are widespread in this area, including the rock masses of Linglong, Luanjiahe, Guojialing, Queshan, Sanfoshan, Duogushan, Wuzhaoshan, Washan, Liudusi, Aishan, and Weideshan [20,21]. They are roughly grouped into four types: Linglong biotite monzogranite, Luanjiahe medium- to coarse-grained granite, Guojialing granodiorite, and Aishan monzogranite. The Linglong biotite monzogranite occurs mainly as batholith, bear-

ing xenolith of the Jiaodong Group and locally showing a gneissic texture [22]. Originating from the partial melting of the Neoarchean lower crust [23], it shows a zonal distribution in the NNE-trending direction between the Jiaojia and Zhaoping faults, with the U-Pb zircon ages of 165–155 Ma [24–26]. The Luanjiahe granite shows zonal distribution in the NNE-trending direction in the middle of the Linglong granite rock masses, with the U-Pb zircon ages of 160–147 Ma [24,27]. The Guoajialing granodiorite intruded the Linglong granitic batholith and metamorphic rocks of Jiaodong Group in stocks in the nearly EW-trending direction with the U-Pb zircon ages of 130–126 Ma [23,28,29], and is divided into the rock masses of Sanshandao, ShangZhuang, Beijie, Congjia, and Guojialing from west to east [17,30]. A wealth of geochemical evidence indicates that the Guojialing granodiorite was sourced from partial melting of the lower crust and mixed with a majority of the mantle material [31]. The Aishan monzogranite intruded the Guojialing granitic pluton in the nearly NE-trending direction with the U-Pb zircon ages of 118–114 Ma [17,29,32].

The Jiaodong gold province is divided into three metallogenic belts, i.e., the Zhaoyuan-Laizhou gold belt in the west, the Penglai-Qixia gold belt in the middle, and the Muping-Rushan gold belt in the east (Figure 1b). The Zhaoyuan-Laizhou gold belt is the largest and contains more than 90% of the Jiaodong Peninsula's gold reserves [6]. Meanwhile, gold deposits in the Zhaoyuan-Laizhou gold belt are mainly hosted in the Mesozoic granitoids or along the contacts between the granitoids and metamorphic rocks, and are typically controlled by NNE- and NE-trending faults that cut the Mesozoic granitoids. There are three ore-controlling fault zones in the Zhaoyuan-Laizhou gold belt, i.e., the Sanshandao-Cangshang, Jiaojia-Xincheng, and Zhaoyuan-Pingdu fault zones from west to east.

3. Geology of the Xiejiagou Gold Deposit

The Xiejiagou gold deposit is located in the Zhaoyuan-Laizhou gold belt (Figure 1), with a reserve of more than 50 t Au [11,33]. The deposit is mainly hosted in the Linglong granite and contains eight discontinuous orebodies (Figure 2). In general, the orebodies strike NNE (15° to 30°), steeply (70° to 80°) dip to SE, and are pinched out and reappeared along both strikes and dips. The average gold grades of the eight orebodies range from 1.62 to 8.90 g/t [34]. The largest orebody, Zone 3, extends about 1500 m in length and more than 500 m in depth, in which pyrite is the most abundant ore mineral, followed by chalcopyrite, galena, natural gold, and electrum, while quartz, sericite, K-feldspar, and calcite are the primary gangue minerals. The lodes are mainly controlled by the NE-trending faults and are cut by the NW-trending fault. The ore-hosting faults are characterized by multiple phases of activity with a compressional metallogenic environment in the early stage and an extensional metallogenic environment in the late stage, presenting an S-shape in plan. The fractured altered rocks in the ore-hosting fault zones are characterized by mylonitization, cataclastic lithification, and structural lenses (Figure 3a,b), reflecting a compressional fracture metallogenic system. Auriferous quartz veins occur usually in fissures of altered-rock-type orebodies (Figure 3c,d). Locally, altered-rock-type ores occur as breccias and were cemented by auriferous quartz veins (Figure 3e,f).

Hydrothermal alteration is widespread in the Xiejiagou gold deposit, mainly including potassic, sericitic, pyritic, and silicic alterations. These alterations are characterized by distinct zonations from orebodies to wall rocks: quartz-pyrite veins → silicification + sericitization + pyritization → K-feldspathization → fresh granite (Figure 4). Based on mineral paragenesis and crosscutting relationships (Figure 5), three stages of mineralization can be distinguished as follows:
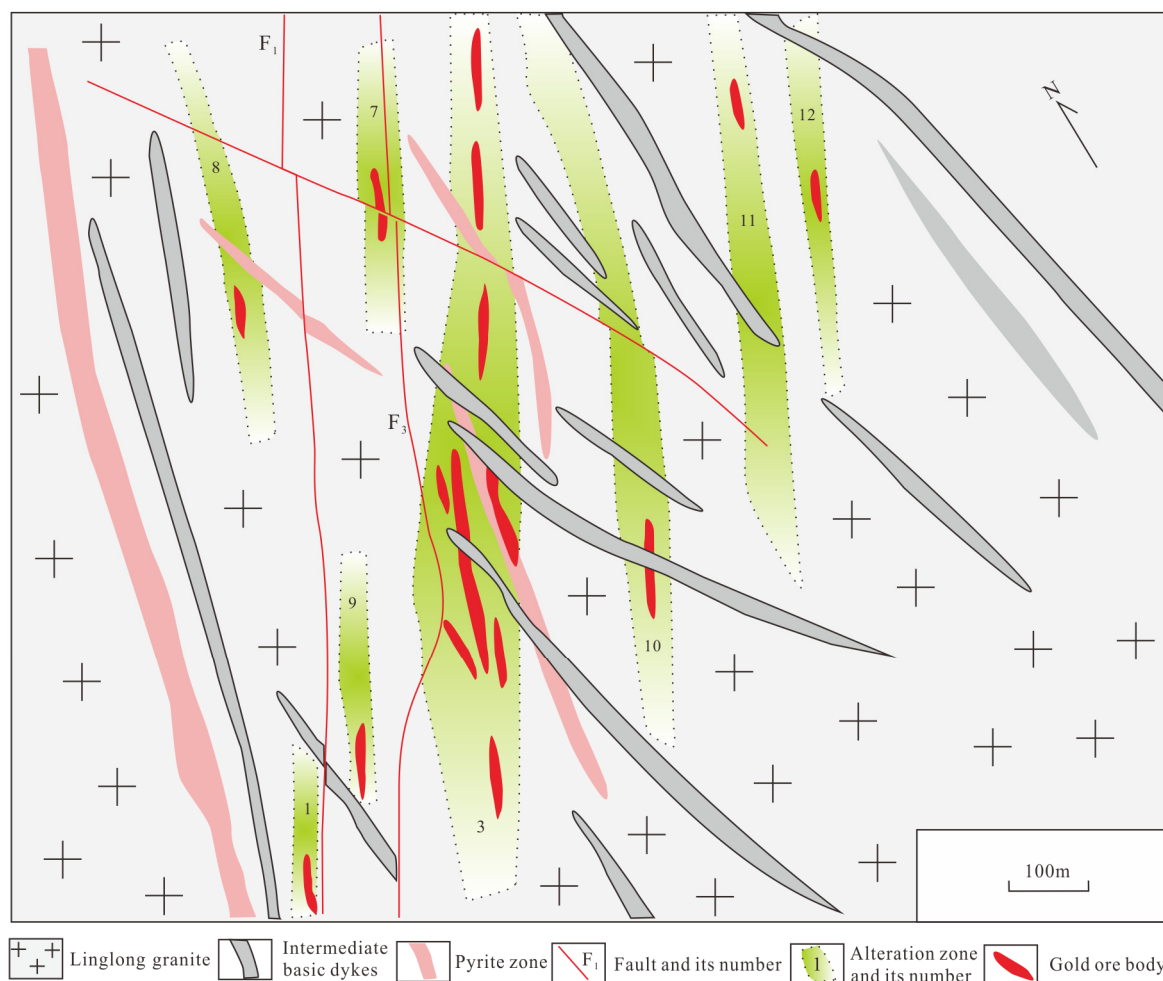
Figure 2. Geological sketch of the Xiejiagou gold deposit (modified after [10]).
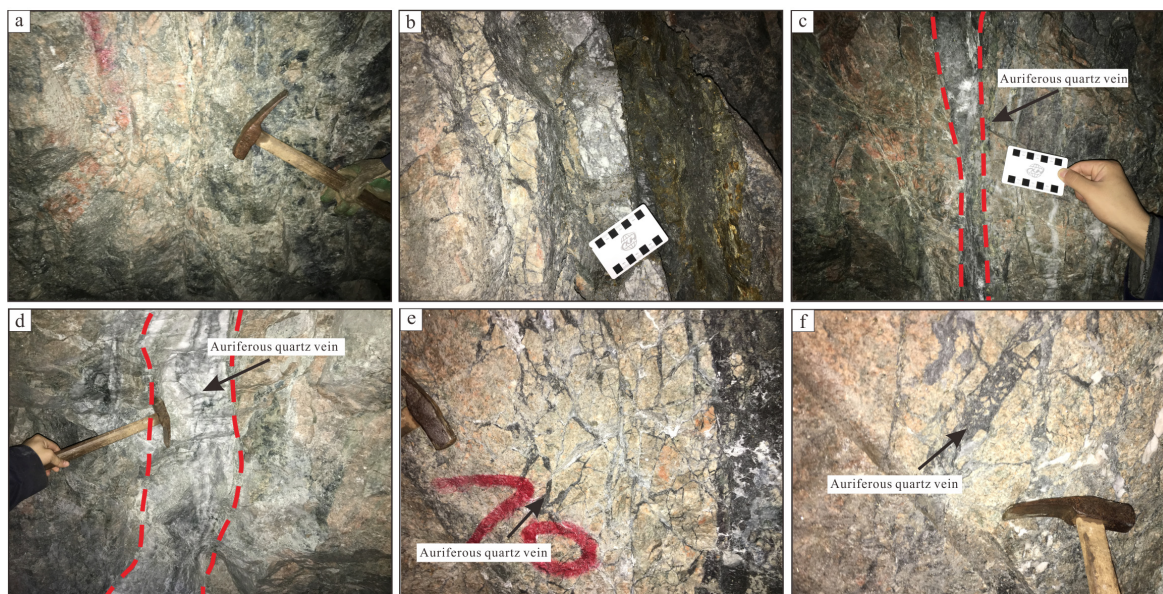

Figure 3. Mineralized types of the Xiejiagou gold deposit. (**a**,**b**) Fractured altered rocks. (**c**,**d**) Auriferous quartz veins interpenetrating fractured altered rocks. (**e**,**f**) Fractured altered rocks in form of breccia cemented by auriferous quartz veins.
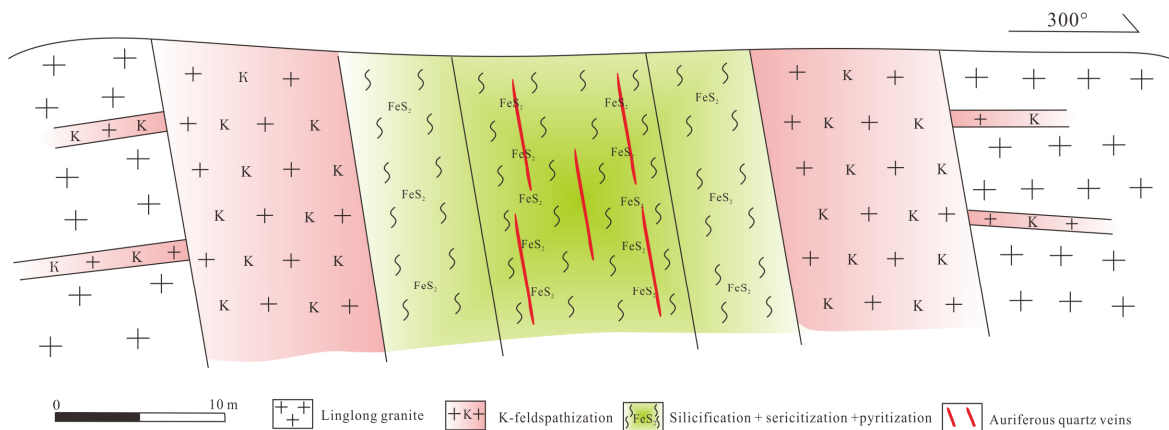
Figure 4. Sketch of mineralized alteration zones in the Xiejiagou gold deposit.

Stage / Mineral	Altered-rock type mineralization		Quartz-vein type mineralization
	Stage I	Stage II	Stage III
Feldspar	▬▬▬		
Quartz	▬▬▬▬▬▬▬▬▬▬▬▬▬▬▬▬		
Sericite		▬▬▬	
Gold	──	▬▬▬	▬▬▬
Pyrite	▬▬▬▬▬▬▬▬▬		▬▬▬
Pyrrhotite			▬▬▬
Chalcopyrite			▬▬▬
Galena			▬▬▬
Sphalerite			▬▬▬
Magnetite			▬▬

Figure 5. Paragenetic sequence for representative hydrothermal minerals of the Xiejiagou gold deposit. The width of the solid lines denotes relative abundance of minerals.

Stage I is characterized by the assemblage of K-feldspar + quartz ± pyrite (Figure 6a). Plagioclase in country rocks is metasomatized by fresh red and blocky K-feldspar (Figure 6a). Quartz (Qz_1) is typically milky white, and occurs mostly as veinlets associated with K-feldspar. Pyrite (Py_1) occurs as coarse-grained cubic crystals sparsely disseminated in quartz. Gold is scarcely precipitated.

Stage II is characterized by the assemblage of sericite + quartz + pyrite (Figure 6b). Sericite is lepidoblastic in texture (Figure 6d,e) and has fully replaced plagioclase and K-feldspar (Figure 6d,e). Quartz (Qz_2) is typically smoky gray to milky white, and occurs mostly coarse grained and disseminated in altered ores (Figure 6b). Pyrite (Py_2) occurs as fine-grained subhedral particles disseminated in altered ores. Disseminated ores with strong sericitization, silicification, and pyritization are the major ore type of this stage, defined as altered-rock-type gold mineralization in this study.

Stage III is characterized by the assemblage of quartz + pyrite ± magnetite. Quartz (Qz_3) is typically smoky gray, and occurs mostly as veins or veinlets (Figure 6c). Pyrite (Py_3) occurs as fine-grained subhedral particles disseminated in quartz (Qz_3). Magnetite is widely developed(Figure 6f,h,i). Visible gold occurs as individual grains situated on pyrite margins (Figure 6g). Mineralization of this stage occurs predominantly at meter- to millimeter-scale veins or veinlets, which are defined as auriferous quartz-vein-type gold

mineralization. Gold grades in the auriferous quartz veins are typically higher than their surrounding altered-rock-type ores.
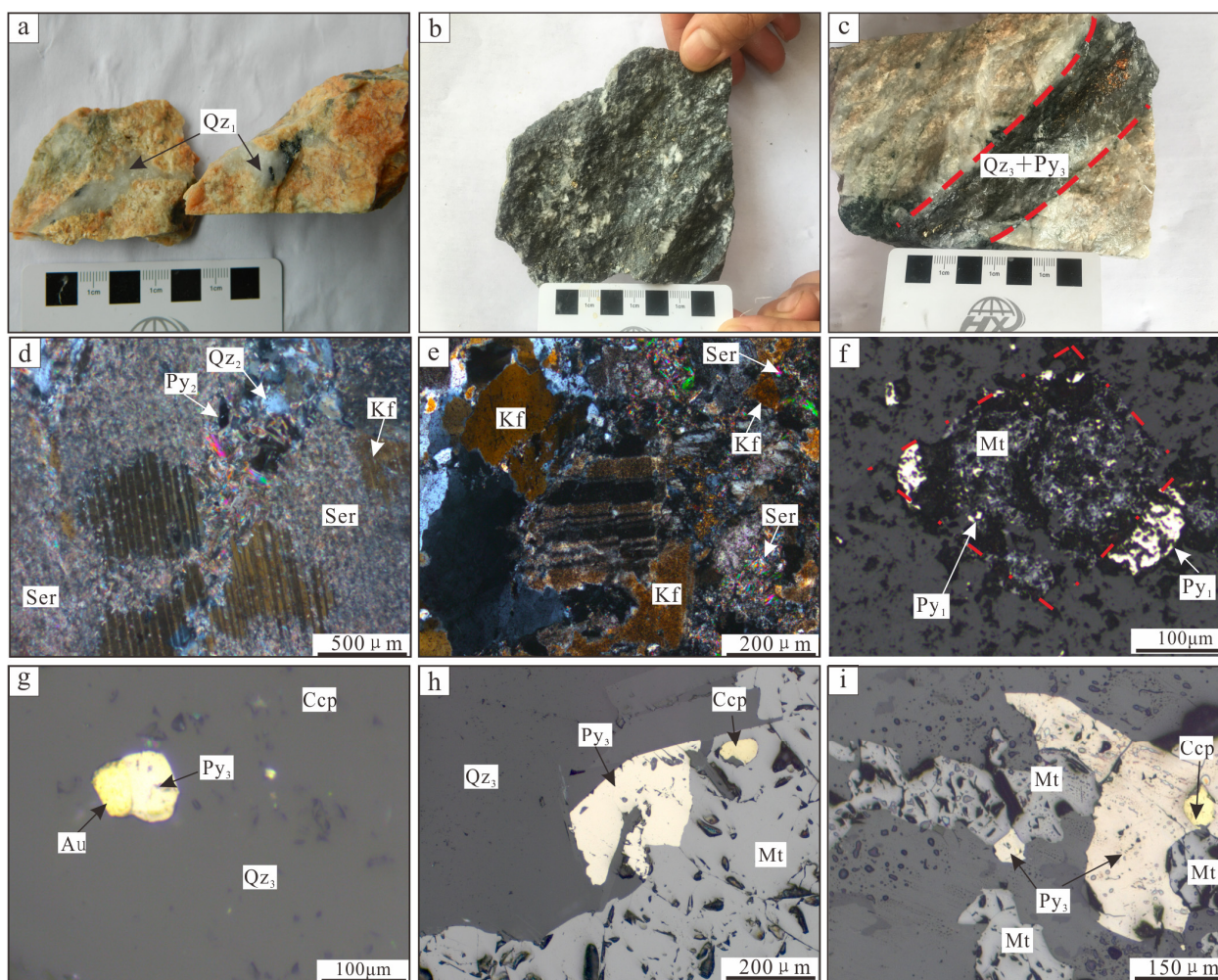

Figure 6. Mineralization-alteration features of the Xiejiagou gold deposit. (**a**–**c**) The hand specimen showing typical K-feldspathization, pyrite–sericite–silicate alteration rock, auriferous quartz veins, respectively. (**d**) Typical pyrite–sericite–silicate alteration rock, including sericite, quartz (Qz$_2$) and pyrite (Py$_2$). (**e**) K-feldspar was metasomatized by sericite. (**f**) Skeleton texture with pyrite (Py1) metasomatized by magnetite. (**g**) Visible gold associated with pyrite (Py$_3$). (**h**) The coexistence of pyrite (Py$_3$) and magnetite with chalcopyrite. (**i**) Pyrite (Py$_3$) metasomatized by magnetite. (**d**,**e**) Photo taken in cross-polarized light. (**f**–**i**) Photos taken in reflected light. Abbreviations: Kf, K-feldspar; Qz$_1$, quartz of stage I; Qz$_2$, quartz of stage II; Qz$_3$, quartz of stage III; Ser, sericite; Mt, magnetite; Py$_1$, pyrite of stage I; Py$_2$, pyrite of stage II; Py$_3$, pyrite of stage III; Au, gold.

4. Sampling and Analytical Methods

Samples in this study were collected from No.3 orebody at the levels of −430 m, −310 m, −350 m, and −230 m above the sea level. Sampling was carried out by taking into account the lateral zonation of alterations and the three-stage evolution of mineralization.

Petrographic and microthermometric studies of fluid inclusions were carried out on 12 quartz samples from three mineralization stages. Microthermometric measurements were performed using a LinkamTHMS600 heating/freezing stage attached to a carl zeiss microscope (Axio Scope A1). After a temperature calibration using artificially synthesized reference samples of fluid inclusions supplied by the American company FLUID INC, the measurement precision of the stage was determined to be ±0.5 °C, ±0.2 °C, and ±2 °C in the temperature ranges of −120 °C to −70 °C, −70 °C to +100 °C, and 100 °C to 500 °C,

respectively. The salinity of CO_2-bearing three-phase inclusions was calculated using the formula proposed by Roedder [35]: $W_{NaCl} = 15.52022 - 1.02342 \times T - 0.05286 \times T^2$, where W_{NaCl} is the mass fraction of NaCl in water solution and *T* is final melting temperature of the clathrate phase ($-9.6\,°C \leq T \leq +10\,°C$). Salinities of liquid–vapor aqueous inclusions and halite-bearing inclusions were calculated using the formulas proposed by Hall et al. [36] and Sterner et al. [37], respectively. Fluid densities of aqueous inclusions and halite-bearing inclusions were calculated using the empirical formulas of Bodnar [38] and Bischoff [39], respectively. The trapping pressures of CO_2-H_2O inclusions were estimated using the program Flincor based on the CO_2-H_2O-NaCl system [40].

Quartz and K-feldspar grains were handpicked from crushings of 40–60 mesh under binocular (>99% purity). Hydrogen–oxygen isotope analysis was performed on the MAT 253 EM mass spectrometer at the Analytical Laboratory of Beijing Research Institute of Uranium Geology (BRIUG), adopting Standard Mean Ocean Water (SMOW) as a standard. Hydrogen isotope analysis was performed through acquisition of the water in inclusions by decrepitation and generation of hydrogen using zinc, with a precision of $\pm 2‰$ for δD. Oxygen isotope analysis was performed by determining oxygen isotope composition in quartz by fluorination (BrF_5) [41], with a precision of $\pm 0.2‰$ for $\delta^{18}O$.

In situ sulfur isotope analysis of pyrite was performed by laser ablation and microanalysis at the State Key Laboratory of Continental Dynamics (Northwest University), during which fs-LA-MC-ICP-MS was employed. This instrument's laser model is Quantronix Integra-He, Ti: Sapphire, triple frequency, an output wavelength of 266 nm, a denudation beam spot of between 15 and 65 μm, a laser frequency of between 5 and 50 Hz, a denudation mode of 3 μm/s line scan, and an HE gas of 0.7 L/min. The sulfur isotope reference materials NBS123, IAEA-S-2, and IAEA-S-3 were used, and their V-CDT values were $\delta^{34}S_{NBS123} = 17.44 \pm 0.28‰$ (2sd), $\delta^{34}S_{IAEA-S-2} = 22.67 \pm 0.22‰$ (2sd), and $\delta^{34}S_{IAEA-S-3} = -32.15 \pm 0.37‰$ (2sd), respectively.

In situ trace-element analysis of pyrite was performed using LA-MC-ICP-MS at Wuhan SampleSolution Analytical Technology Co., Ltd. The trace element composition was calibrated against the glass reference materials BHVO-2G, BCR-2G, and BIR-1G without using an internal stand, and each resolution-based analysis includes about 20 to 30 s of blank signals and 50 s of sample signals. Offline processing (including sample signals and blank signal selection, instrument sensitivity drift calibration, and element content calculation) of the analytical data was performed by ICPMSDataCal software [42].

5. Results

5.1. Fluid Inclusions

5.1.1. Petrography

Based on the petrographic and compositional features of fluid inclusions at room temperature, there types of primary inclusions are recognized in the studied quartz samples, including CO_2-H_2O inclusions (type i), aqueous inclusions (type ii), and daughter mineral-bearing inclusions (type iii).

CO_2-H_2O inclusions (type i) are the most common inclusion type in all quartz samples and contain three or two phases ($L_{CO2} + L_{H2O} \pm V_{CO2}$) at room temperature, with the volumetric proportion of carbonic phases ranging between 15 and 85 vol% (mostly 25–45 vol%). They are typically ellipsoidal, tubular, and negative in shape, and vary in size from 5 to 15 μm (Figure 7a,c,d,f–h). Inclusions with a CO_2 volumetric proportion between 15 and 45 vol% typically homogenized by CO_2-phase disappearance, while inclusions with a CO_2 volumetric proportion between 55 and 85 vol% homogenized by H_2O-phase disappearance.

Aqueous inclusions (type ii) are characterized by a liquid phase and a vapor bubble ($L_{H2O} + V_{H2O}$), vary in size from 5 to 15 μm, and are usually ellipsoidal and tubular in shape (Figure 7b,e). Most aqueous inclusions are liquid-rich (type iia) with a vapor volumetric proportion of 10–45 vol% and homogenized to the liquid phase, while others with a vapor proportion of 55–85 vol% (type iib) homogenized to the vapor phase. In addition, a small

amount of pure-liquid inclusions (type iic) and pure-vapor inclusions (type iid) are also observed.
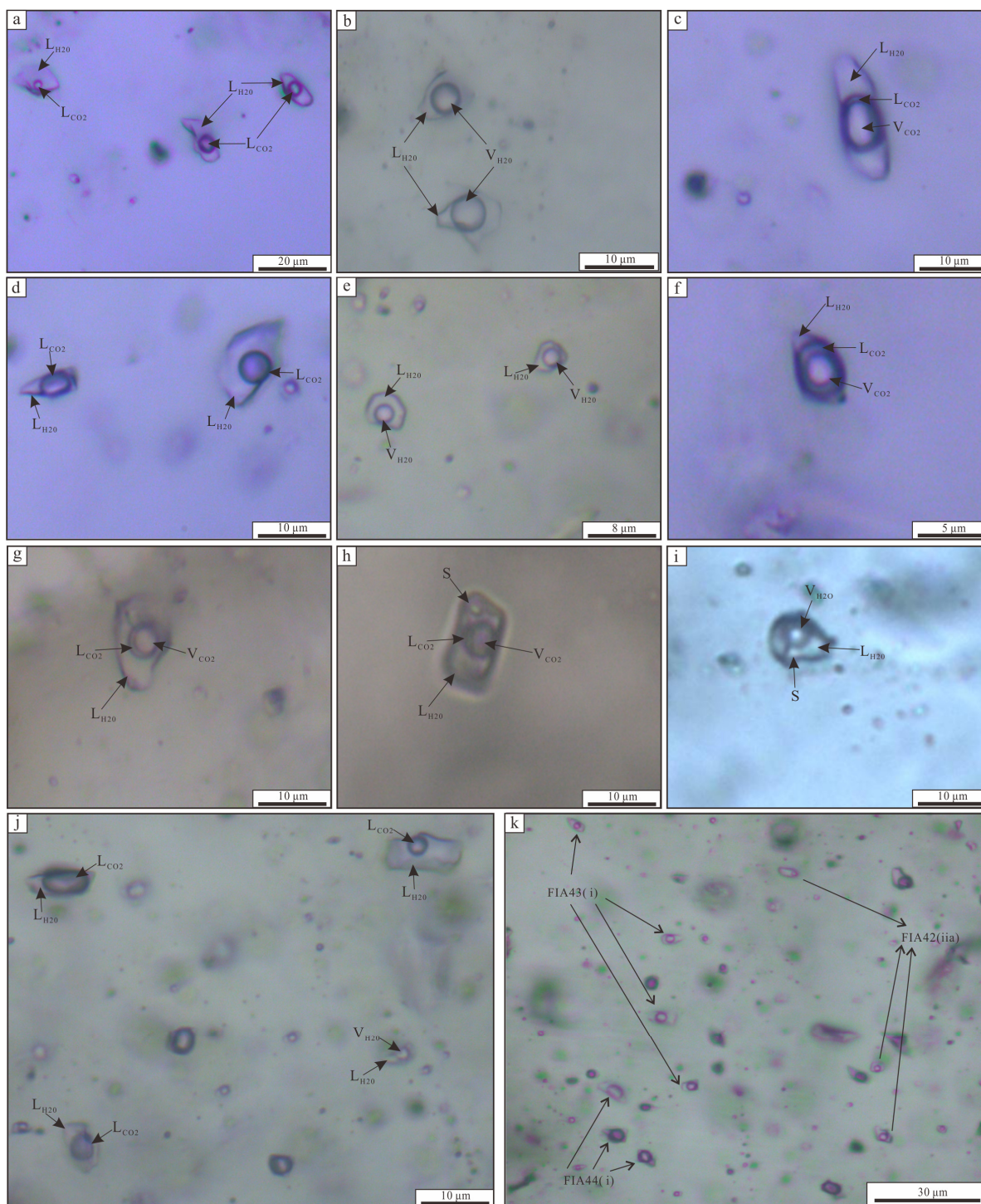
Figure 7. Fluid inclusions in the Xiejiagou gold deposit. (**a**) CO_2-H_2O two-phase inclusion (type i) of stage I. (**b**) Vapor-rich aqueous solution inclusions (type iib) of stage I. (**c**) CO_2-H_2O three-phase inclusion (type i) of stage I. (**d**) CO_2-H_2O two-phase inclusions (type i) of stage II. (**e**) Liquid-rich aqueous solution inclusions (type iia) of stage II. (**f**) CO_2-H_2O three-phase inclusion (type i) of stage II. (**g**) CO_2-H_2O three-phase inclusion (type i) of stage III. (**h**–**i**) Daughter mineral-bearing inclusion (type iii) of stage III. (**j**,**k**) Clustered co-existing liquid-rich aqueous solution inclusions (type iia), CO_2-H_2O inclusions (type i) of stage III.

Daughter mineral-bearing inclusions (type iii) consist of a liquid aqueous phase, a vapor bubble, and a solid phase of daughter mineral ($L_{H2O}+V_{H2O}+S$) at room temperature and vary in size from 5 to 7 μm. The daughter minerals are typically colorless and transparent, cubic in shape, and 1 to 2 μm in diameter (Figure 7h,i), indicating that these daughter minerals should be halite (NaCl). Among six measurements during heating, five daughter minerals were dissolved between 209 °C and 345 °C prior to final homogenization (disappearance of vapor bubble) (Table 1).

Table 1. Microthermometric data of fluid inclusions in the Xiejiagou gold deposit.

Sample	Type	FIA (N)	$T_{m,cla}$ (°C)	$T_{h,CO2}$ (°C)	$T_{m,ice}$ (°C)	$T_{h,tot}$ (°C)	$T_{m,s}$ (°C)	Salinity (wt% NaCleqv)	Density (g/cm³)	Pressure (MPa)
	iia	FIA1 (3)			−4.6−−3.3	311−325		6.4−9.2	0.76−0.77	−
	iib	FIA2 (3)			−4.5−−3.9	339−351		7.6−9.0	0.71−0.75	−
	i	FIA3 (3)	5.0−5.8	29.0−30.0		353−368		7.8−9.1	0.87−0.88	320−335
	i	FIA4 (5)	5.3−7.2	29.9−30.9		327−338		5.4−8.6	0.87−0.90	307−348
	i	FIA5 (5)	5.0−6.3	30.4−30.9		306−319		7.0−9.1	0.86−0.90	294−312
	i	FIA6 (4)	5.8−6.1	29.1−30.5		299−313		7.3−7.8	0.89−0.90	303−317
	i	FIA7 (6)	5.7−6.5	30.1−30.9		273−285		6.6−8.0	0.81−0.83	303−337
Qz₁	i	FIA8 (5)	5.5−5.9	30.3−30.9		293−308		7.6−8.3	0.89−0.91	288−314
	iia	FIA9 (5)			−3.9−−3.7	305−320		7.2−7.6	0.76−0.79	−
	i	FIA10 (3)	5.7−5.9	30.5−30.7		323−337		7.6−8.0	0.85−0.88	291−319
	iib	FIA11 (3)			-5.1−−4.5	323−335		9.0−10.3	0.77−0.78	−
	i	FIA12 (6)	4.7−5.7	30.4−30.9		319−331		8.0−9.5	0.85−0.90	284−331
	iia	FIA13 (3)			−5.3−−4.8	338−341		9.6−10.8	0.75−0.77	−
	i	FIA14 (3)	5.5−6.9	30.1−30.9		347−359		5.9−8.3	0.85−0.86	308−320
	i	FIA15(3)	5.7−6.9	30.8−30.9		280−293		5.9−8.0	0.89−0.91	291−301
	iia	FIA16(4)			−4.3−−3.9	300−303		7.6−8.5	0.79−0.80	−
	iia	FIA17 (3)			−3.5−−3.3	335−348		6.4−6.8	0.70−0.72	−
	iia	FIA18(4)			−3.3−−3.2	285−294		6.2−6.4	0.79−0.80	−
	i	FIA19(3)	6.8−7.1	29.4−29.7		285−297		5.6−6.1	0.91−0.93	304−317
	iia	FIA20(4)			−3.8−−3.4	262−272		6.6−7.4	0.83−0.85	−
	i	FIA21(3)	5.8−7.0	28.9−30.8		304−309		5.8−7.8	0.89−0.92	309−317
Qz₂	i	FIA22 (3)	6.7−7.1	30.5−30.6		273−285		5.6−6.3	0.91−0.92	296−309
	i	FIA23 (3)	4.8−5.3	30.6−30.8		309−323		8.6−9.4	0.85−0.88	276−290
	i	FIA24 (3)	5.6−7.8	30.6−30.8		278−289		4.3−8.1	0.88−0.90	280−286
	i	FIA25 (4)	6.0−7.2	30.4−30.7		291−303		5.4−7.5	0.89−0.91	299−315
	i	FIA26 (4)	5.9−7.0	30.8−30.9		298−307		5.8−7.6	0.88−0.89	298−305
	i	FIA27 (4)	5.8−7.8	30.2−30.9		313−327		4.3−7.8	0.86−0.88	296−311
	iia	FIA28 (5)			−3.5−−3.0	312−327		5.8−6.8	0.73−0.76	−
	i	FIA29 (3)	5.9−6.5	30.8−30.9		311−323		6.6−7.6	0.84−0.87	272−287
	i	FIA30 (4)	5.8−6.6	30.5−30.8		318−325		6.5−7.8	0.81−0.85	238−275
	i	FIA31 (3)	4.8−5.9	30.6−30.9		343−351		7.6−9.4	0.78−0.81	234−253
	iia	FIA32 (5)			−5.1−−4.6	319−333		9.2−10.3	0.76−0.79	−
	i	FIA33 (3)	4.9−5.3	30.6−30.7		351−363		8.6−9.2	0.79−0.81	237−266
	iib	FIA34 (3)			−4.5−−4.2	342−352		8.3−9.0	0.72−0.74	−
	iia	FIA35 (3)			−4.7−−4.5	331−345		9.0−9.4	0.74−0.77	−
	i	FIA36 (4)	4.0−6.3	30.7−30.8		291−304		5.9−8.3	0.86−0.88	270−279
	iib	FIA37 (4)			−4.7−−4.2	364−376		8.3−9.4	0.68−0.71	−
	i	FIA38 (4)	5.1−6.1	30.7−30.9		353−367		7.3−8.9	0.79−0.82	263−280
	iia	FIA39 (4)			−5.2−−4.7	330−338		9.4−10.5	0.77−0.78	−
Qz₃	i	FIA40 (3)	4.0−4.7	30.7−30.8		348−359		9.5−10.6	0.80−0.84	257−280
	iia	FIA41 (3)			−3.2−−3.0	362−369		5.8−6.2	0.65−0.66	−
	iia	FIA42 (3)			−5.2−−5.0	332−340		10.1−10.5	0.76−0.78	−
	i	FIA43 (4)	5.8−6.8	30.1−30.8		327−342		6.1−7.8	0.81−0.87	258−294
	i	FIA44 (3)	5.6−6.1	30.6−30.9		331−344		7.3−8.1	0.74−0.81	241−249
	i	FIA45 (3)	5.1−7.0	30.5−30.7		306−318		5.8−8.9	0.87−0.91	
	i	FIA46 (4)	6.8−7.4	30.6−30.9		290−303		5.1−6.1	0.83−0.89	253−288
	i	FIA47 (3)	5.8−6.4	30.5−30.7		325−329		6.8−7.8	0.85−0.86	278−285
	i	FIA48 (4)	5.6−5.7	30.4−30.7		314−328		8.0−8.1	0.86−0.88	281−301
	i	FIA49 (3)	5.5−7.4	30.5−30.6		329−339		5.1−8.3	0.73−0.85	288−291
	iia	FIA50 (3)			−4.3−−4.2	342−356		8.3−8.5	0.71−0.74	−
	iii	(5)				296−371	209−345	32.4−41.9	1.07−1.11	−

$T_{m,cla}$—Final melting temperature of the clathrate phase for type i fluid inclusions; $T_{h,CO2}$—Temperature of CO_2 (L+V) to CO_2 (L) or CO_2 (V) for type i fluid inclusions; $T_{m,ice}$—Final ice melting temperature; $T_{h,tot}$—Total homogenization temperatures; $T_{m,s}$—Solid dissolution temperature for type iii fluid inclusions.

5.1.2. Microthermometry

In this study, microthermometry was focused on two groups of fluid inclusion assemblages (FIAs), occurring either along quartz growth zones (Figure 8a,b) or as random individuals within quartz grains (Figure 8a). FIAs distributed along a crystal growth zone are used to constrain the homogenization temperature of the inclusions, while fluid inclusion assemblages distributed in an unordered way are considered quasi FIAs [43]. Variations in homogenization temperature for quasi FIAs of this study are relatively small (within 15 °C) and should be acceptable. In addition, for microthermometric measurement, the fluid inclusions are all primary inclusions and develop in undeformed quartz or beside pyrite (Figure 7), and are basically regular in shape with no occurrence of "necking down".
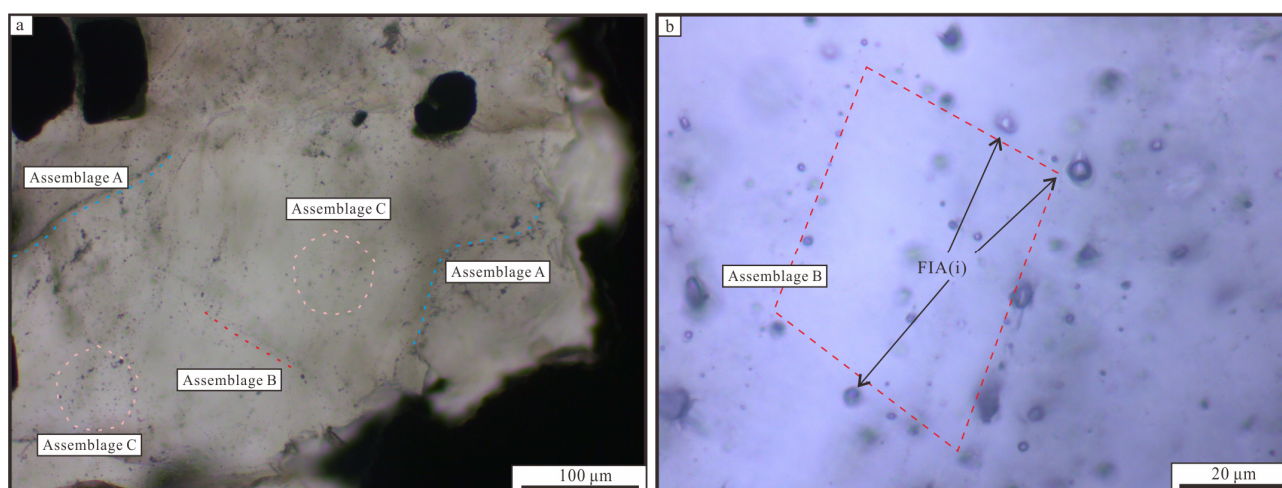

Figure 8. Fluid-inclusion assemblages in the Xiejiagou gold deposit. (**a**) Photomicrograph showing typical assemblage A, B, C; (**b**) Photomicrograph showing typical assemblage B. (Assemblage A), a secondary inclusion assemblage distributed along a healed microfracture; (Assemblage B), a primary inclusion assemblage distributed along a crystal growth zone; (Assemblage C), primary inclusions distributed in an unordered way.

Stage I quartz (Qz_1): This stage comprises mainly primary type i inclusions (Figure 7a,c) and a small number of primary types iia and iib inclusions (Figure 7b). Type i inclusions have a partial homogenization temperature of CO_2 phase ($T_{h,CO2}$) ranging from 29.0 to 30.9 °C to liquid, a total homogenization temperature ranging from 273 to 368 °C, a salinity ranging from 5.4 to 9.5 wt.% NaCl equivalent, and a density ranging from 0.81 to 0.91 g/cm^3, and a pressure ranging from 284 to 348 Mpa. Type iia inclusions have a homogenization temperature ranging from 305 to 341 °C, a salinity ranging from 6.4 to 10.8 wt.% NaCl equivalent, and a density ranging from 0.75 to 0.79 g/cm^3. Type iib inclusions have a homogenization temperature ranging from 323 to 351 °C, a salinity ranging from 7.6 to 10.3 wt.% NaCl equivalent, and a density ranging from 0.71 to 0.78 g/cm^3 (Figure 9, Table 1).
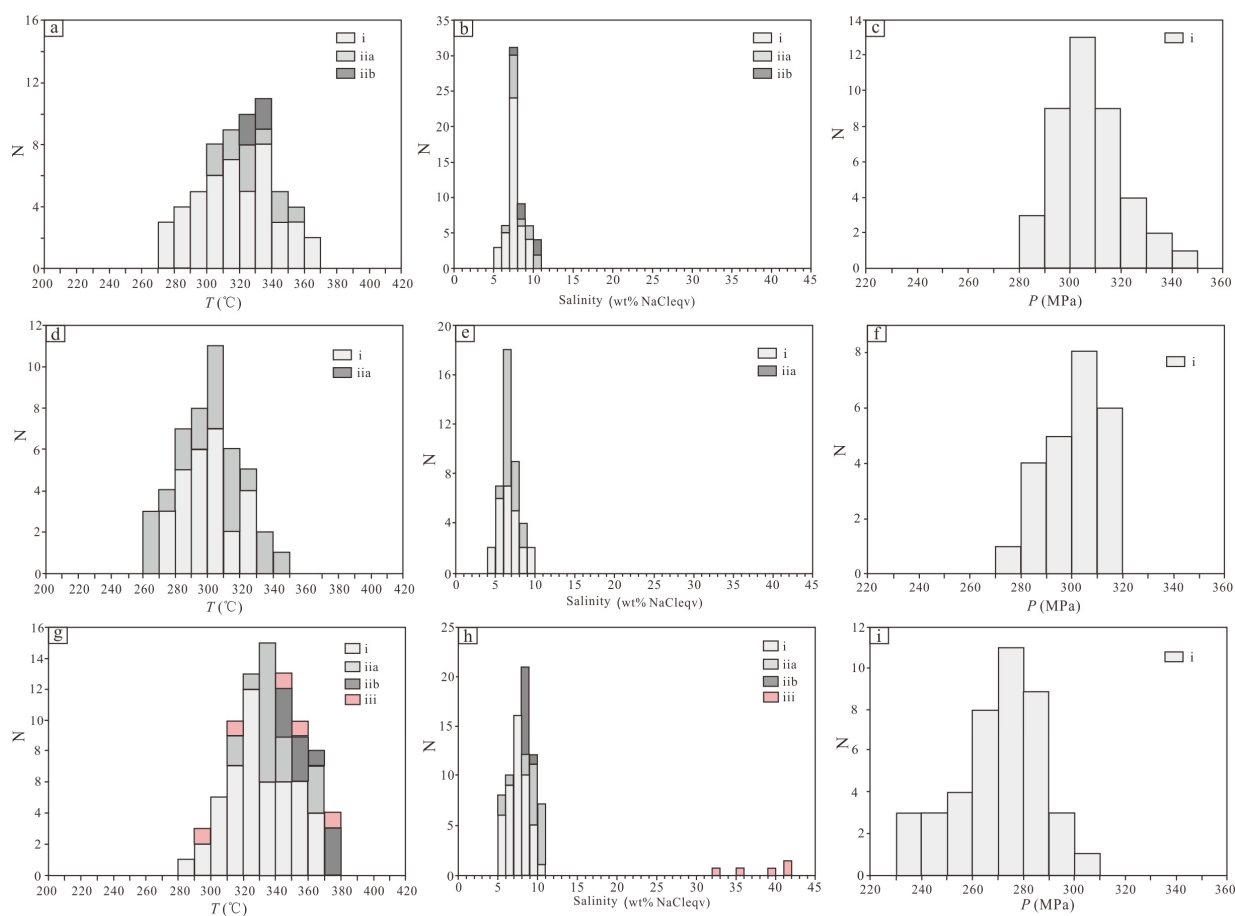
Figure 9. Homogenization temperature, salinity and pressure histograms of fluid inclusions in the Xiejiagou gold deposit. (**a**) Homogenization temperature histogram of fluid inclusions at Stage I. (**b**) Salinity histogram of fluid inclusions at Stage I. (**c**) Pressure histogram of fluid inclusions at Stage I. (**d**) Homogenization temperature histogram of fluid inclusions at Stage II; (**e**) Salinity histogram of fluid inclusions at Stage II. (**f**) Pressure histogram of fluid inclusions at Stage II. (**g**) Homogenization temperature histogram of fluid inclusions at Stage III. (**h**) Salinity histogram of fluid inclusions at Stage III. (**i**) Pressure histogram of fluid inclusions at Stage III.

Stage II quartz (Qz_2): This stage contains inclusion types similar to those of Qz_1 but is less in inclusion quantity. Type i inclusions have a $T_{h,CO2}$ ranging from 28.9 to 30.9 °C to liquid, a total homogenization temperature ranging from 273 to 327 °C, a salinity ranging from 4.3 to 9.4 wt.% NaCl equivalent, a density ranging from 0.85 to 0.93 g/cm³, and a pressure ranging from 276 to 317 Mpa. Type iia inclusions have a homogenization temperature ranging from 262 to 348 °C, a salinity ranging from 5.8 and 8.5 wt.% NaCl equivalent, and a density ranging from 0.70 to 0.85 g/cm³ (Figure 9, Table 1).

Stage III quartz (Qz_3): Compared to Qz_1 and Qz_2, inclusions at this stage are characterized by more types, a larger quantity but smaller sizes. This stage is dominated by types i, iia and iib inclusions, with minor types iii, iic, and iid inclusions. Type i inclusions have a $T_{h,CO2}$ ranging from 30.1 to 30.9 °C to liquid, a total homogenization temperature ranging from 290 to 367 °C, a salinity ranging from 5.1 to 10.6 wt.% NaCl equivalent, a density ranging from 0.73 to 0.91 g/cm³, and a pressure ranging from 234 to 301 Mpa. Type iia inclusions have a homogenization temperature ranging from 319 to 369 °C, a salinity ranging from 5.8 to 10.5 wt.% NaCl equivalent, and a density ranging from 0.65 to 0.79 g/cm³. Type iib inclusions have a homogenization temperature ranging from 342 to 376 °C, a salinity ranging from 8.3 to 9.4 wt.% NaCl equivalent, and a density ranging from 0.68 to 0.74 g/cm³. Type iii inclusions have a homogenization temperature ranging from 296 to 371 °C, a melting temperature of daughter minerals ranging from 209 to 345 °C, a

salinity ranging from 32.4 to 41.9 wt.% NaCl equivalent, and a density ranging from 1.07 to 1.11 g/cm^3 (Figure 9, Table 1).

It is worth noting that fluid immiscibility likely occurred at stage III, as indicated by the widely coexisting type i inclusions with a wide range of L_{H2O}/L_{CO2} ratios and type iia inclusions in the same perspective at room temperature (Figure 7j,k, Table 1) and both having similar homogenization temperatures. For example, the FIA42, FIA43, and FIA44 have narrow homogenization temperatures between 327 and 344 °C (Figure 7k, Table 1). Meanwhile, the assemblages of CO_2-H_2O inclusions with a wide range of L_{H2O}/L_{CO2} ratios have different homogenization forms, see above.

5.2. H-O Isotopes

The H-O isotopic values of 15 quartz samples and 2 K-feldspar samples from the three mineralizing stages in the Xiejiagou deposit are listed in Table 2. The $\delta^{18}O_{H2O}$ values of quartz and K-feldspar were calculated using the formulas $1000\ln\alpha_{quartz-water} = 3.38 \times \frac{10^6}{T^2} - 3.40$ [44] and $1000\ln\alpha_{K-feldspar-water} = 2.91 \times \frac{10^6}{T^2} - 3.41$ [45], where T represents the homogenization temperature of primary FIs from the corresponding hydrothermal stages. As for the quartz of stage I, the δD values vary from −106‰ to −85‰ (average −95‰); the $\delta^{18}O_{H2O}$ values vary from 3.3‰ to 4.4‰ (average 3.8‰). As for the K-feldspar of stage I, the δD values vary from −100‰ to −98‰ (average −99‰); and the $\delta^{18}O_{H2O}$ values vary from 2.7‰ to 3.1‰ (average 2.9‰). As for the quartz of stage II, the δD values vary from −95‰ to −85‰ (average −90‰); and the $\delta^{18}O_{H2O}$ values vary from 0.8‰ to 3.5‰ (average 2.3‰). As for the quartz of stage III, the δD values vary from −98‰ to −89‰ (average −94‰); and the $\delta^{18}O_{H2O}$ values vary from 3.6‰ to 5.7‰ (average 4.5‰).

Table 2. Oxygen and hydrogen isotopes data in the Xiejiagou gold deposit.

Sample	Stage	Mineral	δD (‰)	$\delta^{18}O_{V-SMOW}$ (‰)	$\delta^{18}O_{H2O}$ (‰)
XJG04-4	I	K-feldspar	−100	5.7	2.7
XJG35-1	I	K-feldspar	−98	6.1	3.1
XJG19	I	Qz_1	−106	10.2	3.8
XJG33-2	I	Qz_1	−92	9.9	3.5
XJG22	I	Qz_1	−85	10.8	4.4
XJG12	I	Qz_1	−96	9.7	3.3
XJG28	II	Qz_2	−89	9.4	2.5
XJG07	II	Qz_2	−95	7.7	0.8
XJG42	II	Qz_2	−85	10.4	3.5
XJG23	III	Qz_3	−92	11.3	5.7
XJG37	III	Qz_3	−98	10.3	4.6
XJG03	III	Qz_3	−93	10.4	4.7
XJG04-3	III	Qz_3	−89	10.5	4.8
XJG06	III	Qz_3	−96	9.6	3.9
XJG08	III	Qz_3	−98	9.3	3.6
XJG10	III	Qz_3	−92	10.9	5.2
XJG11	III	Qz_3	−93	9.9	4.2

5.3. In Situ Sulfur Isotope

The in situ sulfur isotope results of 42 point analyses in eight pyrite samples taken from the Xiejiagou deposit are shown in Table 3. The $\delta^{34}S$ values are relatively concentrated, mainly ranging from 5.7‰ to 9.0‰. Specifically, the $\delta^{34}S$ values of pyrite vary from 5.8‰ to 7.2‰ (average 6.4‰) for stages I, 6.6‰ to 9.0‰ (average 7.4‰) for stage II, and 5.7‰ to 7.2‰ (average 6.6‰) for stage III.

Table 3. Sulfur isotope data in the Xiejiagou gold deposit and other typical deposits in the Zhaoyuan-Laizhou gold belt of the Jiaodong gold province.

Name	Sample	Stage	Mineral	$\delta^{34}S_{V\text{-}CDT}$ (‰)	Data Sources
Xiejiagou gold deposit	XJG34-2-1-Py	I	Py_1	5.8	This paper
	XJG34-2-2-Py	I	Py_1	5.8	
	XJG34-2-2-Py-2	I	Py_1	5.9	
	XJG34-2-3-Py	I	Py_1	6.3	
	XJG34-2-3-Py-2	I	Py_1	6.7	
	XJG34-2-4-Py	I	Py_1	6.0	
	XJG34-2-4-Py-2	I	Py_1	6.0	
	XJG50-1-Py	I	Py_1	6.4	
	XJG50-1-Py-2	I	Py_1	6.8	
	XJG50-2-Py	I	Py_1	7.2	
	XJG50-2-Py-2	I	Py_2	7.0	
	XJG42-1-Py	II	Py_2	6.7	
	XJG42-1-Py-2	II	Py_2	6.6	
	XJG42-1-Py-3	II	Py_2	7.3	
	XJG42-2-Py	II	Py_2	7.0	
	XJG42-2-Py-2	II	Py_2	7.1	
	XJG42-3-Py	II	Py_2	7.0	
	XJG42-3-Py-2	II	Py_2	7.1	
	XJG21-1-Py	II	Py_2	7.3	
	XJG21-1-Py-2	II	Py_2	6.7	
	XJG14-2-Py-2	II	Py_2	8.7	
	XJG14-1-Py	II	Py_2	9.0	
	XJG48-1-Py	II	Py_2	7.9	
	XJG48-1-Py-2	II	Py_2	7.9	
	XJG48-2-Py	II	Py_2	7.9	
	XJG48-2-Py-2	II	Py_2	7.3	
	XJG48-2-Py-3	II	Py_2	6.7	
	XJG05-1-Py	III	Py_3	6.7	
	XJG05-1-Py-2	III	Py_3	7.2	
	XJG05-1-Py-3	III	Py_3	6.6	
	XJG06-Py	III	Py_3	6.4	
	XJG06-Py-2	III	Py_3	6.9	
	XJG06-Py-3	III	Py_3	6.9	
	XJG06-2-Py	III	Py_3	7.0	
	XJG06-2-Py-2	III	Py_3	6.7	
	XJG06-2-Py-3	III	Py_3	6.5	
	XJG52-1-Py	III	Py_3	6.7	
	XJG52-1-Py-2	III	Py_3	6.5	
	XJG52-1-Py-3	III	Py_3	6.8	
	XJG52-2-Py	III	Py_3	6.2	
	XJG52-2-Py-2	III	Py_3	6.4	
	XJG52-2-Py-3	III	Py_3	5.7	
Sanshandao deposit	Altered-rock type		Py	9.4−13.0	[3]
Jiaojia gold deposit	Altered-rock type		Py	8.7−11.2	[3]
Xincheng gold deposit	Altered-rock type		Py	5.7−10.6	[46]
Dongfeng gold deposit	Altered-rock type		Py	5.7−10.6	[47]
Jiuqu gold deposit	Altered-rock type		Py	7.5−7.8	[3]
	Auriferous quartz-vein type		Py	7.3−8.2	

Table 3. *Cont.*

Name	Sample	Stage	Mineral	$\delta^{34}S_{V\text{-}CDT}$ (‰)	Data Sources
Taishang gold deposit	Altered-rock type		Py	4.5−8.6	[3,9]
	Auriferous quartz-vein type		Py	5.9−9.0	
Wangershan gold deposit	Altered-rock type		Py	6.3−8.7	[9]
	Auriferous quartz-vein type		Py	6.6−8.6	
Luoshan/ Fushan gold deposits	Altered-rock type		Py	4.3−7.5	
	Auriferous quartz-vein type		Py	4.7−7.2	

5.4. In Situ Trace Elements

The trace elements values of pyrite determined by LA-ICP-MS in the Xiejiagou deposit are listed in Table 4. Twenty-four point analyses were conducted, including seven Py_1, six Py_2, and eleven Py_3. With the exception of metallization-related elements (Au, Ag, and Bi), the contents of other elements (Cu, Pb, Zn, Co, Ni, As, Sb, Te, W, Sn, and Mo) are generally higher than their detection limits. Au contents in Py_1, Py_2 and Py_3 are <DBL–0.061 ppm, 0.001–0.729 ppm and <DBL–0.363 ppm, respectively. As contents in Py_1, Py_2, and Py_3 are 0.153–305 ppm, 10.8–29.3 ppm, and 1.81–15.0 ppm, respectively. Co/Ni ratios in Py_1, Py_2 and Py_3 are 0.90–1.73, 0.11–8.39 and 1.04–36.46, respectively. Sb/Bi ratios in Py_1, Py_2 and Py_3 are 0.079–1964, 0.002–0.093 and 0.001–0.526, respectively. As/Ag ratios in Py_1, Py_2 and Py_3 are 1.89–3626, 1.34–171 and 3.12–433, respectively. As shown in the trace elements correlation diagram (Figure 10), Au does not correlate with As, Pb, Zn, and Cu, but positively correlates with Ag and Bi, suggesting that Au is most closely related to Ag and Bi in the Xiejiagou deposit. As shown in the comparative box plot (Figure 11), from Py_1 to Py_2 to Py_3, the contents of Au, Ag and Bi tend to initially increase and then decrease; As, Cu and Zn gradually decrease; and W, Sn and Mo tend to first decrease and then increase.
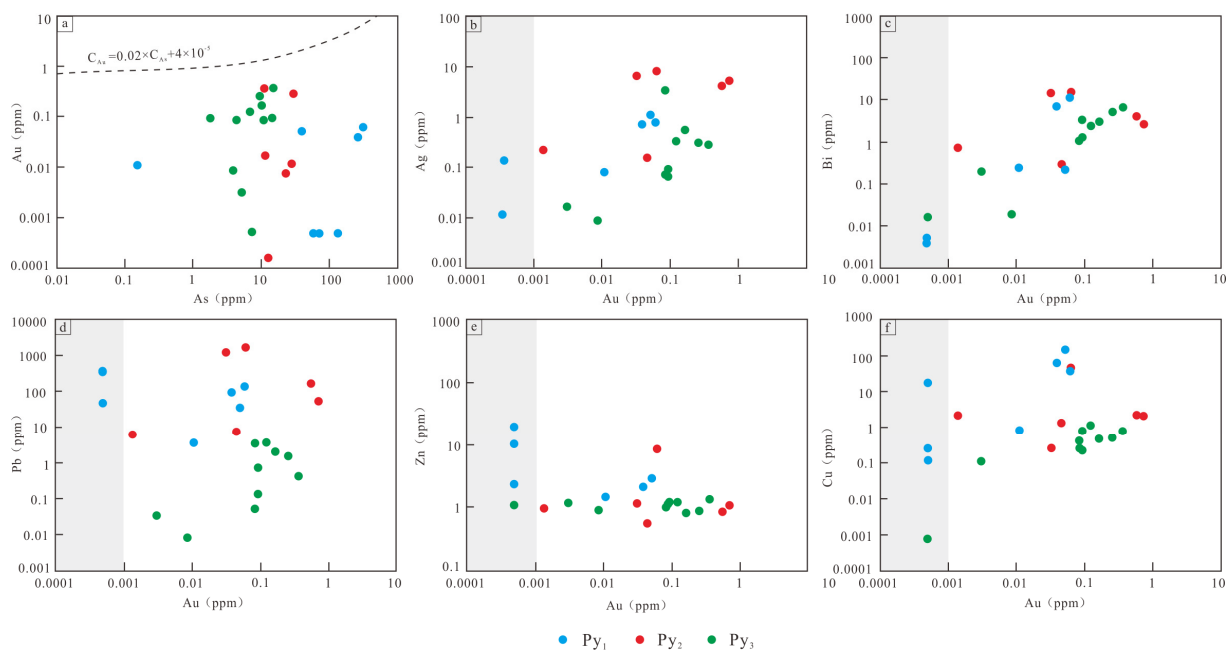

Figure 10. Correlation diagram of trace elements of pyrite in the Xiejiagou gold deposit. (**a**) Au vs. As, the formula of gold saturation curve: $C_{Au} = 0.02 \times C_{As} + 4 \times 10^{-5}$ [48]; (**b**) Au vs. Ag; (**c**) Au vs. Bi; (**d**) Au vs. Pb; (**e**) Au vs. Zn; (**f**) Au vs. Cu. the values in gray areas are less than detection limits.
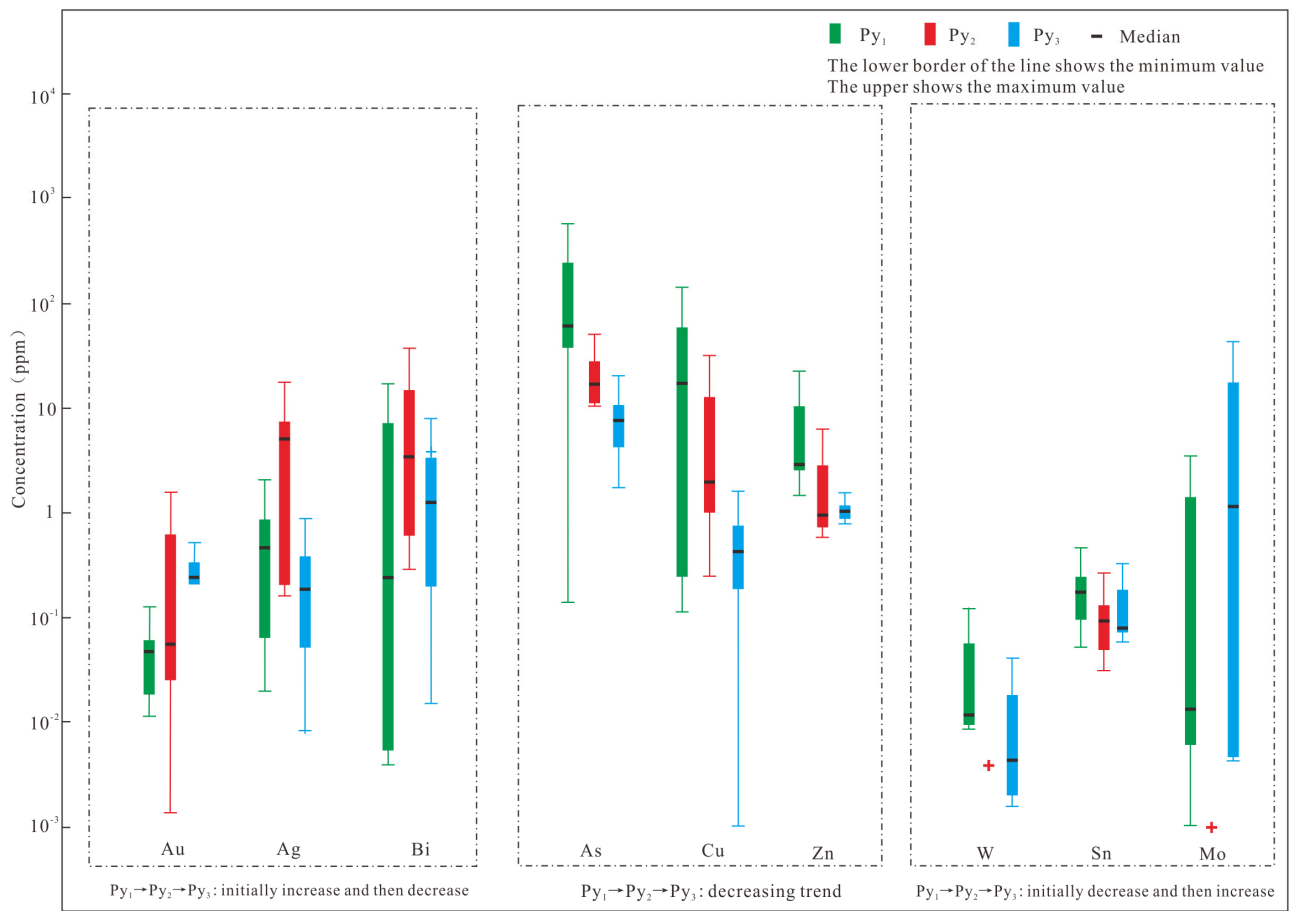
Figure 11. Comparative box plot of trace element concentrations of pyrite in the Xiejiagou gold deposit.

Table 4. Trace elements composition of pyrite determined by LA-ICP-MS in the Xiejiagou gold deposit.

Sample	Stage	Mineral	Au	Ag	As	Sb	Co	Ni	Cu	Pb	Zn	Bi	W	Sn	Mo	Co/Ni	Sb/Bi	As/Ag
values/the detection limit			ppm/The lower limit of detection values 0.001 ppm															
XJG14-01	I	Py_1	DBL	0.227	130	0.362	4.33	4.10	18.0	48.6	20.4	4.61	0.011	0.299	0.022	1.06	0.079	572
XJG14-02	I	Py_1	0.011	0.081	0.153	0.021	4.57	4.81	0.857	3.58	1.53	0.247	0.014	0.118	0.001	0.95	0.085	1.89
XJG14-03	I	Py_1	0.039	0.727	255	0.864	1.89	2.09	60.0	94.1	2.23	7.06	0.012	0.232	0.014	0.90	0.122	350
XJG14-04	I	Py_1	0.061	0.794	305	1.71	5.14	3.74	38.3	136	8.70	11.2	0.010	0.216	0.012	1.37	0.153	384
XJG30-01	I	Py_1	0.052	1.12	38.3	0.454	8.94	5.18	149	35.9	3.06	0.215	BDL	0.055	0.006	1.73	2.112	34.2
XJG27-1-01	I	Py_1	DBL	0.019	68.9	9.82	BDL	BDL	0.255	360	10.5	0.005	0.097	0.115	2.01	—	1964	3626
XJG27-1-02	I	Py_1	DBL	BDL	55.9	9.04	BDL	95.7	0.116	319	2.47	0.004	0.112	0.035	1.41	—	—	—
XJG21-01	II	Py_2	0.063	8.45	11.3	0.178	104	12.4	46.2	1619	8.20	16.1	BDL	0.095	BDL	8.39	0.011	1.34
XJG21-02	II	Py_2	0.001	0.228	12.5	0.069	64.7	20.8	2.14	6.14	0.973	0.743	BDL	0.126	BDL	3.11	0.093	54.8
XJG42-01	II	Py_2	0.576	4.21	29.3	0.031	89.5	12.3	2.07	166	0.835	4.19	0.004	0.032	BDL	7.28	0.007	6.96
XJG42-02	II	Py_2	0.729	5.34	10.8	0.005	162	118	2.03	55.6	1.06	2.72	BDL	0.146	0.00	1.37	0.002	2.02
XJG42-03	II	Py_2	0.045	0.161	27.6	0.026	22.4	22.7	1.31	7.27	0.571	0.295	BDL	BDL	BDL	0.99	0.088	171
XJG42-04	II	Py_2	0.032	6.83	22.5	0.059	4.47	40.7	0.248	1227	1.15	15.1	BDL	0.065	BDL	0.11	0.004	3.29
XJG50-01	III	Py_3	0.122	0.334	6.77	0.027	378	365	1.17	3.71	1.21	2.42	0.005	0.059	36.3	1.04	0.011	20.3
XJG50-02	III	Py_3	0.093	0.088	1.81	0.003	624	79.8	0.760	0.77	1.18	3.30	2.62	0.202	5.49	7.82	0.001	20.6
XJG50-03	III	Py_3	0.256	0.311	9.54	0.015	1344	116	0.520	1.57	0.886	5.06	0.016	0.182	22.3	11.59	0.003	30.7
XJG50-04	III	Py_3	0.163	0.553	10.3	0.004	533	156	0.465	2.06	0.818	2.95	0.018	0.192	2.32	3.42	0.001	18.6
XJG05-1-01	III	Py_3	0.091	0.065	14.6	DBL	1907	52.3	0.218	0.14	1.10	1.30	0.002	0.072	BDL	36.46	—	—
XJG05-1-02	III	Py_3	0.008	0.009	3.90	0.010	44.9	10.4	BDL	0.009	0.905	0.019	BDL	0.073	0.005	4.32	0.526	433
XJG05-1-03	III	Py_3	DBL	BDL	7.39	0.002	381	97.4	0.001	BDL	1.08	0.016	BDL	0.079	BDL	3.91	—	—
XJG06-01	III	Py_3	0.083	0.071	4.38	0.001	439	38.1	0.259	0.055	0.971	1.09	0.003	0.130	BDL	11.52	0.001	61.7
XJG06-02	III	Py_3	0.363	0.289	15.0	DBL	1739	350	0.789	0.448	1.33	6.63	0.002	0.101	0.004	4.97	—	—
XJG06-03	III	Py_3	0.083	3.46	10.8	0.036	768	262	0.417	3.51	1.05	1.08	BDL	0.069	0.005	2.93	0.033	3.12
XJG06-04	III	Py_3	0.003	0.016	5.22	DBL	676	231	0.114	0.037	1.17	0.200	0.004	0.076	0.009	2.93	—	—

DBL: not detected.

6. Discussion

6.1. Origin and Evolution of Ore-Forming Fluids

A large number of studies in recent years show that the initial fluids of gold deposits in the Jiaodong area are mainly magmatic water and contain some meteoric water in the middle and late metallogenic stages [5,10,13,49–53]. As shown in the δD-δ^{18}O diagram (Figure 12), the H-O isotopes of quartz and K-feldspar fall between the magmatic water zone and the meteoric water line, but closer to the magmatic water line, indicating that the ore-forming fluids in the Xiejiagou gold deposit were dominated by magmatic water and mixed with minor meteoric water. Secondary fluid inclusions generally can result in inaccurate δD and δO values for the fluids, causing the calculated δD and δO values to be slightly lower than those of the original ore-forming fluids [54,55]. Quartz samples in the Xiejiagou gold deposit contain a small amount of secondary fluid inclusions (Figure 8a). Therefore, the true δD and δO values of the ore-forming fluids in the Xiejiagou gold deposit are closer to the range of magmatic water. It also further indicates that the ore-forming fluids are mixed with very little meteoric water. This inference for the origin of the fluids is also supported by the following evidences. (1) The δ^{13}C$_{PDB}$ ($-4.5‰$ to $-5.4‰$) ratios and δ^{18}O$_{SMOW}$ values ($4.2‰$ to $6.5‰$) of calcite in the Xiejiagou gold deposit [11] are primarily in the range of magmatic-derived carbon [56,57]. (2) Sulfides in the Xiejiagou gold deposit show Pb isotope composition (^{206}Pb/^{204}Pb = 17.251–17.315, ^{207}Pb/^{204}Pb = 15.486–15.519, and ^{208}Pb/^{204}Pb = 37.904–38.029), overlapping with the composition of whole rocks from Mesozoic granites and dikes, indicating a similar Mesozoic lead reservoir [58] and suggesting that the ore-forming fluids are closely related to the deep-sourced magmatic fluids. (3) Although the low salinity and high CO_2 content in the fluid inclusions show strong similarities to metamorphic fluids [59,60], the fact that late Archean to early Proterozoic regional metamorphism identified in the study area [61–63] significantly predates the formation of the Xiejiagou gold deposit and the lack of early Cretaceous metamorphism strongly precludes the involvement of metamorphic fluid. This conclusion is consistent with previous studies that the Precambrian metamorphism has no genetic role to play in the formation of the Mesozoic gold mineralization in the Jiaodong area [64,65]. (4) As shown in the Ni-Co and Sb/Bi-As/Ag diagram, most pyrite samples of the Xiejiagou gold deposit fall between magmatic-related and hydrothermal-related pyrites (Figure 13a) or magmatic-related pyrite (Figure 13b), rather than metamorphic hydrothermal-related pyrite [66–68]. Therefore, it can be inferred that the Xiejiagou gold deposit belongs to intrusion-related gold deposits.
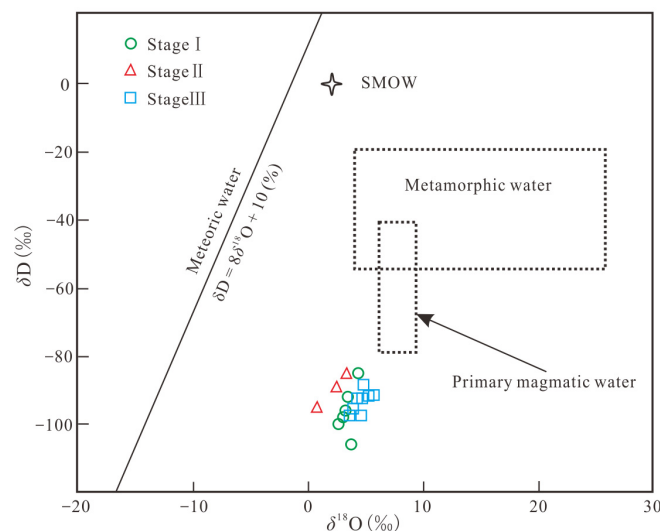

Figure 12. δD and δ^{18}O characteristics of the ore-forming fluids in the Xiejiagou gold deposit [69]. The meteoric water line from [70].
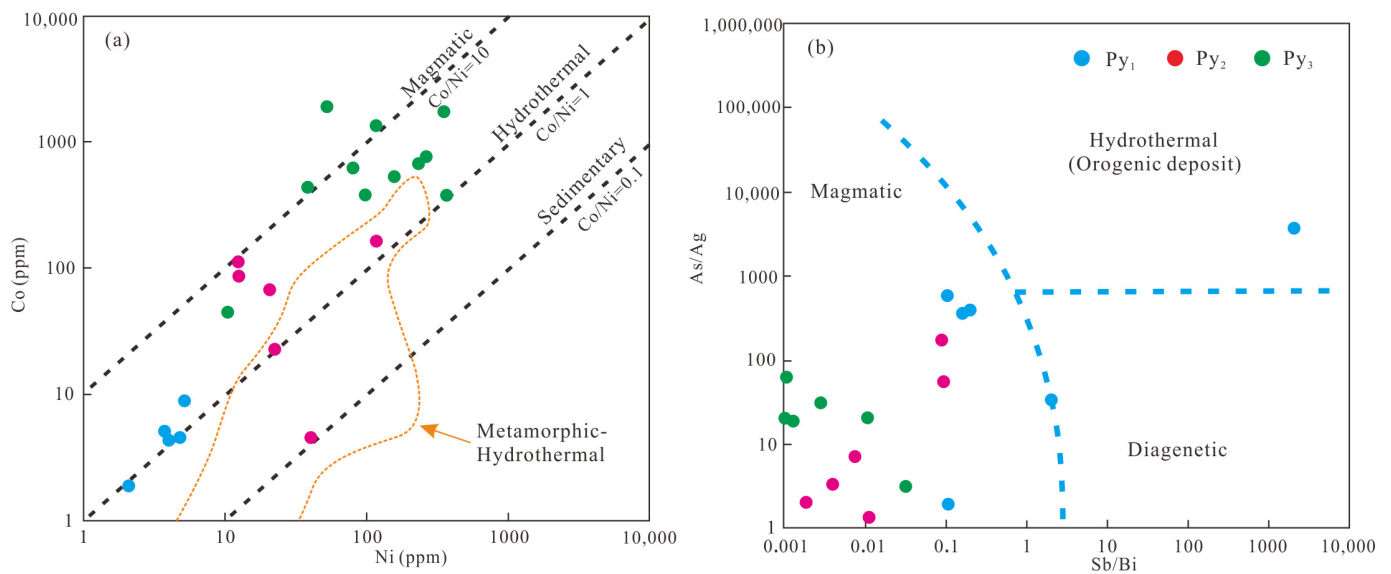
Figure 13. (**a**) Co vs. Ni in pyrite, modified after [66–68]; (**b**) As/Ag vs. Sb/Bi in pyrite, modified after [67].

Microthermometric data show that the ore-forming fluids of altered-rock-type mineralization (stages I and II) have moderate-to-high homogenization temperature (262 to 368 °C) and low-to-moderate salinity (4.3 to 10.8 wt.% NaCl equivalent). From stage I to stage II, the homogenization temperature gradually decreases, while the salinity changes only a little. In contrast, daughter mineral-bearing inclusions (32.4 to 41.9 wt.% NaCl equivalent) are found in auriferous quartz-vein mineralization (stage III). The ore-forming fluids of stage III have slightly higher homogenization temperature (290 to 376 °C) and obviously higher salinity (5.1 to 41.9 wt.% NaCl equivalent) than fluids from stages I and II (Figure 9). Variations in the bulk fluid composition from multiple hydrothermal events usually cause several stages of sulfide precipitation with distinct sulfur isotopes, irregular boundaries and/or corrosion textures between alternating bands [71,72]. Therefore, it can be inferred from the following facts that the two distinct gold mineralization types in the Xiejiagou gold deposit may reflect two separate mineralization events. (1) H-O isotopes do not exhibit the trend of moving towards the meteoric water line from early stages (stages I and II) to the late stage (stage III), and are even closer to the magmatic water zone at stage III (Figure 12). (2) Homogenization temperature and high-temperature element (W, Sn, and Mo) concentrations in pyrite first decrease and then increase (Figures 9 and 11). (3) δ^{34}S values and metallization-related element (Au, Ag, and Bi) concentrations in pyrite first increase and then decrease (Figures 11 and 14). (4) Late-stage (III) auriferous quartz veins usually superimpose on the early-stage (stages I and II) altered-rock-type mineralization (Figure 3c,d), and there are corrosion textures between the two distinct mineralization types (Figure 6f).

6.2. Transition of Metallogenic Environment from Early to Late Stages

Altered-rock-type mineralization (stages I and II) in the Xiejiagou gold deposit is characterized by fractured altered rocks with mylonitization, cataclastic lithification, and structural lenses (Figure 3a,b), typical of a compressional fracture metallogenic system [73]. In contrast, auriferous quartz veins typically occur in fissures of altered-rock-type orebodies (Figure 3c,d). Locally, the altered-rock-type ore breccias were cemented by the auriferous quartz veins (Figure 3e,f), reflecting an extensional metallogenic system in the late-stage mineralization (stage III). Chen et al. [74] proposed that, as responses to the continuous shifts in the drifting direction of the Pacific Plate, the Jiaodong Terrane had experienced an extensional regime between 135 and 122 Ma, a brief compressional transitional period around 122 to 120 Ma, and a return to the extensional regime between 120 and 110 Ma

(e.g., [6,75,76]). Mineralization of the Xiejiagou gold deposit occurred in 122 to 118 Ma [11]. Therefore, the deposit may have undergone a transition from a compressional environment to an extensional environment during mineralization, resulting in an apparent superimposition of auriferous quartz veins on altered-rock-type orebodies (Figures 3c,d and 6c). This inference is also evidenced by the instantaneous pressure fluctuation from early to late stages in the Xiejiagou gold deposit. As indicated by the estimated trapping pressures of inclusions (Figure 9c,f,h), stage III formed at obviously lower pressure (234–301 MPa, average = 271 MPa) than stage I (284–348 MPa, average = 308 MPa) and stage II (276–317 MPa, average = 301 MPa).

Along with the metallogenic transition from a compressional environment to an extensional environment, the hydrothermal system of the Xiejiagou gold deposit also experienced a transition from a relatively reduced to a relatively oxidized state. The occurrence of magnetite in the auriferous quartz veins (Figure 6h,i) is strong evidence supporting the increasing oxidation state of the ore-forming fluids (e.g., [6,77,78]).

6.3. Comparison of Gold Occurrence State and Deposition for the Two Distinct Mineralization Types

In terms of occurrence state, two types of gold are recognized in the Xiejiagou gold deposit: invisible and visible gold. As revealed by LA-ICP-MS analysis of trace elements in pyrite, invisible gold distributes in Py_1, Py_2, and Py_3. However, the gold content in all of them is low (Table 4) and below the gold solubility line in the Au-As correlation diagram (Figure 10a) [48,79], indicating that invisible gold in pyrite likely presents as solid solution (Au^{1+}). Comparatively, visible gold grains can only be observed in Py_3 (Figure 6g) from the auriferous quartz veins. Combined with research on visible gold occurring primarily in fissures formed at the stage of pyrite–quartz veins in the Xiejiagou gold deposit [80], it can be concluded that the visible gold was mainly formed from the auriferous quartz-vein-type mineralization.

Hydrothermal alteration is widespread in the altered-rock-type mineralization (stages I and II), and much more intense than that in the auriferous quartz-vein-type mineralization (stage III) in the Xiejiagou gold deposit. It can be observed that feldspar of Linglong granite was transformed into K-feldspar during hydrothermal K-feldspathization, and K-feldspar was transformed to sericite and quartz during hydrothermal sericitization and silicification (Figure 6d,e). This implies that intense water–rock interaction occurred between ore-forming fluids and wall rocks in the altered-rock-type mineralization, which is supported by sulfur isotope and fluid inclusions petrography. $\delta^{34}S$ values of pyrite in the Xiejiagou gold deposit for altered-rock-type and auriferous quartz-vein-type mineralization ranging from 5.8‰ to 9.0‰ and 5.7‰ to 7.2‰, respectively. No sulfates are found at Xiejiagou, and pyrite is the predominant sulfur-bearing mineral in altered-rock-type and auriferous quartz-vein-type mineralization. The $\delta^{34}S$ values of pyrite at each stage are relatively concentrated (Figure 14). Specifically, there is a very slight variation of sulfur isotopic compositions (within 1.5 ‰) in a single pyrite grain (Table 3). Therefore, it can be inferred that isotopic fractionation between sulfide pairs would have been negligible during the mineralization processes and the $\delta^{34}S$ values of pyrite can represent the bulk sulfur isotopic compositions of the ore-forming fluids in the Xiejiagou deposit [81–83]. Although we could not determine the nature of the sulfur reservoir from the isotopic data from the Xiejiagou gold deposit, the $\delta^{34}S$ values of pyrite from altered-rock-type mineralization and auriferous quartz-vein-type mineralization in the Xiejiagou gold deposit are similar to those of other similar gold deposits in the Zhaoyuan-Laizhou gold belt (Figure 14). It is proven that the increasing of $\delta^{34}S$ values for the altered-rock-type gold deposits in the Zhaoyuan-Laizhou gold belt is mainly controlled by water–rock reaction (e.g., [1,5,7]) and sulfur isotopic composition equilibrating between ore-forming fluids and country rocks ($\delta^{34}S$ values of Linglong granites: 6.1‰–10.1‰ [84]; $\delta^{34}S$ values of Guojialing granites: 2.7‰–10.0‰ [85]; Figure 14a). Accordingly, the gradually increasing $\delta^{34}S$ values (from 5.8‰–7.2‰ to 6.6‰–9.0‰) for altered-rock-type gold mineralization in the Xiejiagou gold

deposit can also be explained by water–rock interaction and gradually equilibrating with the $\delta^{34}S$ values of country rocks (Linglong granites) (Figure 14). In addition, altered-rock-type gold mineralization is characterized by type i fluid inclusions and immiscible inclusions that have not been observed, indicating that there was no widespread phase separation or boiling in this mineralization. In contrast, the occurrence of immiscible inclusions in auriferous quartz veins shows that fluid immiscibility was an important factor controlling gold precipitation. In general, when CO_2-rich ore-forming fluids entered an open space and were affected by fault-valve or hydraulic fracturing, phase separation took place and resulted in fluid immiscibility. The stability of the fluids was disrupted when H_2S and CO_2 were released from the liquid phase to the vapor phase (e.g., [47,86–89]). Subsequently, Au precipitated from the ore-forming fluids. This is evidenced by the transition of the metallogenic environment from early to late stage in the Xiejiagou gold deposit.

In summary, the altered-rock-type mineralization resulted from intense water–rock interaction between the fluids and wall rocks, while the precipitation of gold in auriferous quartz veins was caused by fluid immiscibility in response to pressure fluctuations in the open space.
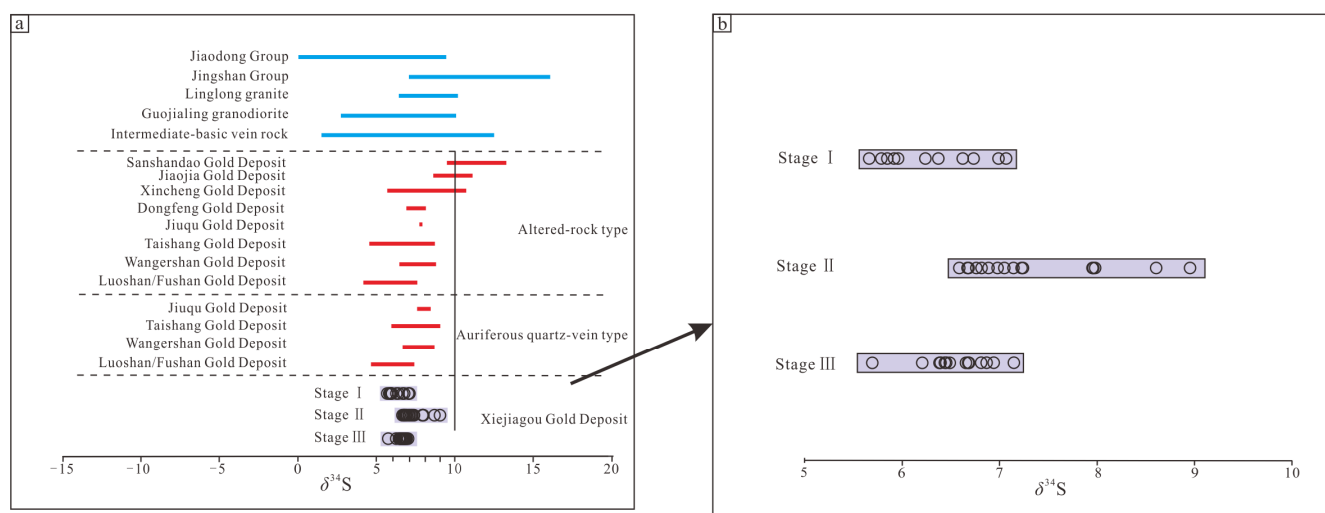

Figure 14. Comparative characteristics of sulfur isotopic composition of typical gold deposits and main geologic blocks in the northwest Jiaodong Peninsula (**a**) and sulfur isotopic composition of pyrite in the Xiejiagou gold deposit (**b**). The data of Jiaodong Group, Jingshan Group, Linglong Granite, Guojialing Granite, and intermediate-basic dykes are derived from [84,85,90].

6.4. Implications for a Two-Stage Superimposed Gold Mineralization

During the mineralization process, some early-stage pyrite grains (Py_1) were dissolved by the late-stage magnetite (skeleton texture) (Figure 6f), which was strong evidence that previously crystallized pyrite was reworked by the late-stage ore-forming fluids. Mills et al. [91] proposed that fluid-assisted dissolution and reprecipitation of previously crystallized Au-bearing pyrite can remobilize Au and drive it into structurally and/or chemically favorable sites. In particular, the oxidation state of the late-stage mineralizing fluids is high, which will transfer Au^0 into Au^{1+} or Au^{3+}, promoting further enrichment of gold in fluids to form high-grade gold mineralization [73]. Therefore, the fact that gold grades in the auriferous quartz veins are typically higher than their surrounding altered-rock-type ores in the Xiejiagou gold deposit reflects a late-stage superimposed gold mineralization on the early stage, with oxidizing ore-forming fluids reworking previously crystallized pyrite and remobilizing its internal gold for further enrichment of gold.

Although some gold deposits in the Zhaoyuan-Laizhou gold belt also host both altered-rock-type and auriferous quartz-vein-type gold mineralization in one single deposit, these two types of mineralization typically spatially separate. The altered rocks are in deeper

space, whereas the quartz veins are in upper space [92]. This distribution pattern can be attributed to local fault attributes, such as the dip angles of the faults [73] or the properties of the faults (first-order regional faults, or subsidiary second-order faults) [47], indicating that both occurrences of altered rocks and quartz veins in a single deposit were the result of a faulting system on a single mineralization event [6]. However, altered-rock-type mineralization and auriferous quartz-vein-type mineralizations in the Xiejiagou gold deposit are spatially superimposed and reflect two separate mineralization events that should be in response to the temporal transition of the regional stress field from compression to extension (discussed in detail in Section 6.2). This metallogenic feature also responds well to an abrupt change in drift direction of the subducting Pacific Plate [75,76]. Consequently, by recording a transition of a compressional–extensional (closed–open) metallogenic environment and a two-stage superimposed gold mineralization at the Xiejiagou suggest that the regional tectonic shift at ca. 120 Ma previously reported in the gold deposits of the Penglai-Qixia gold belt [6] may have played a key role in gold mineralization in the Zhaoyuan-Laizhou gold belt.

7. Conclusions

(1) The Xiejiagou gold deposit shows unique two-stage gold mineralization, with an early-stage altered-rock-type mineralization (Jiaojia type) superimposed by a late-stage auriferous quartz-vein-type mineralization (Linglong type).

(2) The ore-forming fluids were of magmatic origin, and very little meteoric water was involved in the formation of the Xiejiagou gold deposit. The discontinuous evolution trends of H-O isotopes, sulfur isotopes, homogenization temperatures, metallization-related element (Au, Ag, and Bi) concentrations, and the differences in salinity of fluid inclusions from early stages (I and II) to the late stage (III) show the two distinct types of gold mineralization in the Xiejiagou gold deposit may be two separate mineralization events.

(3) The altered-rock-type mineralization resulted from intense water–rock interaction between the fluids and wall rocks, while the precipitation of gold in auriferous quartz veins was caused by fluid immiscibility. In addition, oxidizing ore-forming fluids in the auriferous quartz reworked early stage crystallized pyrite and remobilize its internal gold for further enrichment of gold.

(4) The Xiejiagou gold deposit uniquely records a metallogenic environmental transition from compressional, reduced to extensional, oxidized at ca. 120 Ma, which corresponds well with the regional tectonic shift during this time period. It can be inferred that the regional tectonic shift at ca. 120 Ma may have played a key role in gold mineralization in the Zhaoyuan- Laizhou gold belt.

References

1. Song, M.C.; Yang, L.Q.; Fan, H.R.; Yu, X.F.; Ding, Z.J.; Zhang, Y.W.; Qiu, K.F.; Li, J.; Zhang, L.; Wang, B.; et al. Current progress of metallogenic research and deep prospecting of gold deposits in the Jiaodong Peniusula during 10 years for Exploration Breakthrough Strategic Action. *Geol. Bull. China* **2022**, *41*, 903–935. (In Chinese with English abstract)
2. Qiu, K.F.; Goldfarb, R.J.; Deng, J.; Yu, H.C.; Gou, Z.Y.; Ding, Z.J.; Wang, Z.K.; Li, D.P. Gold Deposits of the Jiaodong Peninsula, Eastern China. *SEG Special Publ.* **2020**, *23*, 753–773.

3.   Qiu, K.F.; Deng, J.; Laflamme, C.; Long, Z.Y.; Wan, R.Q.; Moynier, F.; Yu, H.C.; Zhang, J.Y.; Ding, Z.J.; Goldfarb, R.J. Giant Mesozoic gold ores derived from subducted oceanic slab and overlying sediments. *Geochim. Cosmochim. Acta* **2023**, *343*, 133–141. [CrossRef]

4.   Qiu, Y.S.; Wang, K.H.; Yang, G.H. *Regional Metallogenetic Setting of the Zhaoyuan-Yexian Areas in Shandong Province*; Liaoning Science and Technology Press: Shenyang, China, 1988; pp. 1–291. (In Chinese)

5.   Wen, B.J.; Fan, H.R.; Hu, F.F.; Liu, X.; Yang, K.F.; Sun, Z.F. Fluid evolution and ore genesis of the giant Sanshandao gold deposit, Jiaodong gold province, China: Constrains from geology, fluid inclusions and H-O-S-He-Ar isotopic compositions. *J. Geochem Explor.* **2016**, *171*, 96–112. [CrossRef]

6.   Yang, K.F.; Jiang, P.; Fan, H.R.; Zuo, Y.B.; Yang, Y.H. Tectonic transition from a compressional to extensional metallogenic environment at ∼120 Ma revealed in the Hushan gold deposit, Jiaodong, North China Craton. *J. Asian Earth Sci.* **2018**, *160*, 408–425. [CrossRef]

7.   Fan, H.R.; Lan, T.G.; Li, X.H.; Santosh, M.; Yang, K.F.; Hu, F.F.; Feng, K.; Hu, H.L.; Peng, H.W.; Zhang, Y.W. Conditions and processes leading to large-scale gold deposition in the Jiaodong province, eastern China. *Sci. China Earth Sci.* **2021**, *64*, 1504–1523. (In Chinese with English abstract) [CrossRef]

8.   Mills, S.E.; Tomkins, A.G.; Weinberg, R.F.; Fan, H.R. Anomalously silver-rich vein-hosted mineralisation in disseminated-style gold deposits, Jiaodong gold district, China. *Ore Geol. Rev.* **2015**, *68*, 127–141. [CrossRef]

9.   Guo, L.N. Metallogenic Mechanism of the Jiaodong-Type Gold Deposit, Shandong Province, China. Ph.D. Thesis, China University of Geosciences (Beijing), Beijing, China, 2016; pp. 36–146. (In Chinese with English abstract)

10. Ding, D.S.; Chen, L.; Gong, E.P.; Shi, W.G.; Shao, Z.W.; Zhang, Y.L. Fluid Inclusion Study and Metallogenic Mechanism of Xiejiagou Gold Deposit in Shandong Province. *Miner. Depos.* **2017**, *36*, 345–363. (In Chinese with English abstract)

11. Ma, W.D.; Fan, H.R.; Liu, X.; Yang, K.F.; Hu, F.F.; Zhao, K.D.; Cai, Y.C.; Hu, H.L. Hydrothermal fluid evolution of the Jintingling gold deposit in the Jiaodong peninsula, China: Constraints from U-Pb age, CL imaging, fluid inclusion and stable isotope. *J. Asian Earth Sci.* **2018**, *160*, 287–303. [CrossRef]

12. Wei, Y.G.; Wang, J.G.; Deng, J.; Zhang, Z.Q.; Lin, J.Z.; Yan, S.L. Study on the Fluid Inclusions from Xiejiagou Gold Deposit in Shandong and Its Geological Significance. *Geoscience* **2005**, *19*, 224–230. (In Chinese with English abstract)

13. Fan, H.R.; Zhai, M.G.; Xie, Y.H.; Yang, J.H. Ore-forming fluids associated with granite-hosted gold mineralization at the Sanshandao deposit, Jiaodong gold province, China. *Miner. Depos.* **2003**, *38*, 739–750. [CrossRef]

14. Feng, L.Q.; Gu, X.X.; Zhang, Y.M.; Wang, J.L.; Ge, Z.L.; He, Y.; Zhang, Y.S. Geology and geochronology of the Shijia gold deposit, Jiaodong Peninsula, China. *Ore Geol. Rev.* **2020**, *120*, 103432. [CrossRef]

15. Zhou, T.H.; Lü, G.X. Tectonics, granitoids and Mesozoic gold deposits in East Shandong, China. *Ore Geol. Rev.* **2000**, *16*, 71–90. [CrossRef]

16. Guo, J.H.; Chen, F.K.; Zhang, X.M.; Siebel, W.; Zhai, M.G. Evolution of syn- to post-collisional magmatism from north Sulu UHP belt, eastern China: Zircon U–Pb geochronology. *Acta Petrol. Sin.* **2005**, *21*, 1281–1301. (In Chinese with English abstract)

17. Yang, K.F.; Fan, H.R.; Santosh, M.; Hu, F.F.; Wilde, S.A.; Lan, T.G.; Lu, L.N.; Liu, Y.S. Reactivation of the Archean lower crust: Implications for zircon geochronology, elemental and Sr-Nd-Hf isotopic geochemistry of late Mesozoic granitoids from northwestern Jiaodong Terrane, the North China Craton. *Lithos* **2012**, *146–147*, 112–127. [CrossRef]

18. Qiu, J.S.; Wang, D.Z.; Luo, Q.H.; Liu, H. ^{40}Ar/^{39}Ar dating of volcanic rocks from the Qingshan Formation in the Jiaolai basin, eastern Shandong province: A case study of the Fenlingshan Volcanic Apparatus in Wulian county. *J. China Univ. Geosci.* **2001**, *7*, 351–355. (In Chinese with English abstract)

19. Li, J.W.; Paulo, V.; Zhou, M.F.; Zhao, X.F.; Ma, C.Q. Geochronology of the Pengjiakuang and Rushan gold deposits, eastern Jiaodong gold province, northeastern China: Implications for regional mineralization and geodynamic setting. *Econ. Geol.* **2006**, *101*, 1023–1038.

20. Fan, H.R.; Hu, F.F.; Yang, J.H.; Shen, K.; Zhai, M.G. Fluid Evolution and Large-Scale Gold Metallogeny during Mesozoic Tectonic in the Eastern Shandong Province. *Acta Petrol. Sin.* **2005**, *21*, 1317–1328. (In Chinese with English abstract)

21. Lu, L.N.; Fan, H.R.; Hu, F.F.; Yang, K.F.; Lan, T.G. Emplacement Depth of the Guojialing Granodiorites from the Northwestern Jiaodong Peninsula, Eastern China: Evidences from Hornblende Thermobarometry and Fluid Inclusions. *Acta Petrol. Sin.* **2010**, *27*, 1521–1532. (In Chinese with English abstract)

22. Wang, L.G.; Qiu, Y.M.; McNaughton, N.J.; Groves, D.I.; Luo, Z.K.; Huang, J.Z.; Miao, L.C.; Liu, Y.K. Constraints on crustal evolution and gold metallogeny in the northwestern Jiaodong Peninsula, China, from SHRIMP U-Pb zircon studies of granitoids. *Ore Geol. Rev.* **1998**, *13*, 275–291. [CrossRef]

23. Hou, M.L.; Jiang, Y.H.; Jiang, S.Y.; Ling, H.F.; Zhao, K.D. Contrasting origins of late Mesozoic adakitic granitoids from the northwestern Jiaodong Peninsula, east China: Implications for crustal thickening to delamination. *Geol. Mag.* **2007**, *144*, 619–631. [CrossRef]

24. Zhang, J.; Zhao, Z.F.; Zheng, Y.F.; Dai, M.N. Postcollisional magmatism: Geochemical constraints on the petrogenesis of Mesozoic granitoids in the Sulu orogen, China. *Lithos* **2010**, *119*, 512–536. [CrossRef]

25. Jiang, N.; Chen, J.Z.; Guo, J.H.; Chang, G.H. In situ zircon U-Pb, oxygen and hafnium isotopic compositions of Jurassic granites from the North China Craton: Evidence for Triassic subduction of continental crust and subsequent metamorphism-related ^{18}O depletion. *Lithos* **2012**, *142–143*, 84–94. [CrossRef]

26. Ma, L.; Jiang, S.Y.; Dai, B.Z.; Jiang, S.H.; Hou, M.L.; Pu, W.; Xu, B. Multiple sources for the origin of Late Jurassic Linglongadakitic granite in the Shandong peninsula, eastern China: Zircon U-Pb geochronological, geochemical and Sr-Nd-Hf isotopic evidence. *Lithos* **2013**, *162–163*, 251–263.

27. Chen, J.; Sun, F.Y.; Wang, L.; Wang, S.; Li, R.H. Zircon U-Pb Geochronology and Petrogeochemistry of Luanjiahe Granite in Jiaodong Region and Their Geological Significance. *Glob. Geol.* **2015**, *34*, 283–295. (In Chinese with English abstract)

28. Yang, J.H.; Zhu, M.F.; Liu, W.; Zhai, M.G. Geochemistry and Petrogenesis of Guojialing Granodiorites from the Northwestern Jiaodong Peninsula, Eastern China. *Acta Petrol. Sin.* **2003**, *19*, 692–700. (In Chinese with English abstract)

29. Zhang, L.; Liu, Y.; Li, R.H.; Huang, T.; Zhang, R.Z.; Chen, B.H.; Li, J.K. Lead Isotope Geochemistry of Dayingezhuang Gold Deposit, Jiaodong Peninsula, China. *Acta Petrol. Sin.* **2014**, *30*, 2468–2480. (In Chinese with English abstract)

30. Chen, G.J.; Sun, F.Y.; Li, Y.C.; Liu, K. U-Pb Dating, Geochemical Characteristics and Geological Significance of Guojialing Grandiorite in Jiaodong Peninsula. *Glob. Geol.* **2014**, *33*, 39–47. (In Chinese with English abstract)

31. Li, X.H.; Fan, H.R.; Hu, F.F.; Hollings, P.; Yang, K.F.; Liu, X. Linking lithospheric thinning and magmatic evolution of Late Jurassic to Early Cretaceous granitoids in the Jiaobei Terrane, southeastern North China Craton. *Lithos* **2019**, *324–325*, 280–296. [CrossRef]

32. Goss, S.C.; Wilde, S.A.; Wu, F.Y.; Yang, J.H. The age, isotopic signature and significance of the youngest Mesozoic granitoids in the Jiaodong Terrane, Shandong Province, North China Craton. *Lithos* **2010**, *120*, 309–326. [CrossRef]

33. Wang, J.G.; Zhang, Z.Q.; Deng, J.; Zhai, Y.S.; Yan, S.L.; Zhang, J.; You, S.N. Geologic features and origin type of Xiejiagou gold deposit—A new breakthrough in the area of Jiaodong gold deposit geology research and prospecting. *Gold* **2006**, *11*, 9–13. (In Chinese with English abstract)

34. Sun, L. Study on the Fluid Inclusions of Xiejiagou Gold Deposit. Master's Thesis, China University of Geosciences (Beijing), Beijing, China, 2006; pp. 1–55. (In Chinese with English abstract)

35. Roedder, E. Fluid inclusions. *Miner. Soc. Am. Rev. Miner.* **1984**, *12*, 644.

36. Hall, D.L.; Stern, S.M.; Bodnar, R.J. Freeing point depression of NaCl-KCl-H_2O solutions. *Econ. Geol.* **1988**, *83*, 197–202. [CrossRef]

37. Sterner, S.M.; Hall, D.L.; Bodnar, R.J. Synthetic Fluid Inclusion. V. Solubility Relation in the System NaCl-KCl-H_2O under Vapor-Saturated Conditions. *Geochim. Cosmochim. Acta* **1988**, *52*, 989–1005. [CrossRef]

38. Bodnar, R.J. Revised equation and table for determining the freezing point depression of H_2O-NaCl solution. *Geochim. Cosmochim. Acta* **1993**, *57*, 683–684. [CrossRef]

39. Bischoff, J.L. Densities of liquids and vapors in boiling NaCl-H_2O solutions A PVTX summary from 300 °C to 500 °C. *Am. J. Sci.* **1991**, *291*, 309–338. [CrossRef]

40. Brown, P.E. FLINCOR: A microcomputer program for the reduction and investigation of fluid-inclusion data. *Am. Mineral.* **1989**, *74*, 1390–1393.

41. Clayton, R.N.; Mayeda, T.K. The use of bromine pentafluoride in the extraction of oxygen from oxides and silicates for isotopic analysis. *Geochim. Cosmochim. Acta* **1963**, *27*, 43–52. [CrossRef]

42. Liu, Y.S.; Hu, Z.C.; Gao, S.; Günther, D.; Xu, J.; Gao, C.G.; Chen, H.H. In situ analysis of major and trace elements of anhydrous minerals by LA-ICP-MS without applying an internal standard. *Chem. Geol.* **2008**, *257*, 34–43. [CrossRef]

43. Chi, G.X.; Lu, H.Z. Validation and representation of fluid inclusion microthermometric data using the fluid inclusion assemblage (FIA) concept. *Acta Petrol. Sin.* **2008**, *24*, 1945–1953. (In Chinese with English abstract)

44. Clayton, R.N.; O'Neil, J.R.; Mayeda, T.K. Oxygen isotope exchange between quartz and water. *J. Geophys. Res.* **1972**, *77*, 3057–3067. [CrossRef]

45. O'Neil, J.R.; Taylor, H.P. The Oxygen and Cation Exchange Chemistry of Feldspars. *Am. Mineral.* **1967**, *152*, 198–201.

46. Zhang, C.; Liu, Y.; Liu, X.D.; Feng, J.Q.; Huang, T.; Zhang, Q.; Wang, X.D. Characteristics of sulfur isotope geochemistry of the Xincheng gold deposit, Northwest Jiaodong, China. *Acta Petrol. Sin.* **2014**, *30*, 2495–2506. (In Chinese with English abstract)

47. Wen, B.J.; Fan, H.R.; Santosh, M.; Hu, F.F.; Pirajno, F.; Yan, K.F. Genesis of two different types of gold mineralization in the Linglong gold field, China: Constrains from geology, fluid inclusions and stable isotope. *Ore Geol. Rev.* **2015**, *65*, 643–658. [CrossRef]

48. Reich, M.; Kesler, S.; Utsunomiya, S.; Palenik, C.S.; Chryssoulis, S.L.; Ewing, R.C. Solubility of gold in arsenian pyrite. *Geochim. Cosmochim. Acta* **2005**, *69*, 2781–2796. [CrossRef]

49. Hu, F.F.; Fan, H.R.; Shen, K.; Zhai, M.G.; Jin, C.W.; Chen, X.S. Nature and evolution of ore-forming fluids in the Rushan lode gold deposit, Jiaodong peninsula of eastern China. *Acta Petrol. Sin.* **2005**, *21*, 1329–1338. (In Chinese with English abstract)

50. Hou, M.L.; Jiang, S.Y.; Shen, K.; Lian, J.G.; Liu, Q.C.; Xiao, F.L. Fluid inclusion and H-O isotope study of gold mineralization in the Penglai gold field, Eastern Shandong. *Acta Petrol. Sin.* **2007**, *23*, 2241–2256. (In Chinese with English abstract)

51. Cai, Y.C.; Fan, H.R.; Hu, F.F.; Yang, K.F.; Lan, T.G.; Yu, H.; Liu, Y.M. Ore-forming fluids, stable isotope and mineralizing age of the Hubazhuang gold deposit, Jiaodong Peninsula of eastern China. *Acta Petrol. Sin.* **2011**, *27*, 1341–1351. (In Chinese with English abstract)

52. Jiang, X.H.; Fan, H.R.; Hu, F.F.; Yang, K.F.; Lan, T.G.; Zheng, X.L.; Jin, N.X. Comparative studies on fluid inclusion in different depths and ore genesis of the Sanshandao gold deposit, Jiaodong Peninsul. *Acta Petrol. Sin.* **2011**, *27*, 1327–1340. (In Chinese with English abstract)

53. Yao, X.F.; Cheng, Z.Z.; Du, Z.Z.; Pang, Z.S.; Yang, Y.Q.; Liu, K. Petrology, Geochemistry, and Sr-Nd-S Isotopic Compositions of the Ore-Hosting Biotite Monzodiorite in the Luanjiahe Gold Deposit, Jiaodong Peninsula, China. *J. Earth Sci.-China* **2021**, *32*, 51–67. [CrossRef]

54. Goldfarb, R.J.; Groves, D.I. Orogenic gold: Common or evolving fluid and metal sources through time. *Lithos* **2015**, *233*, 2–26. [CrossRef]

55. Guo, L.N.; Goldfarb, R.J.; Wang, Z.L.; Li, R.H.; Chen, B.H.; Li, J.L. A comparison of Jiaojia- and Linglong-type gold deposit ore-forming fluids: Do they differ? *Ore Geol. Rev.* **2017**, *88*, 511–533. [CrossRef]

56. Deines, P.; Harris, J.W.; Robinson, D.N.; Gurney, J.J.; Shee, S.R. Carbon and oxygen isotope variations in diamond and graphite eclogites from Orapa, Botswana, and the nitrogen content of their diamonds. *Geochim. Cosmochim. Acta* **1991**, *55*, 515–524. [CrossRef]

57. Cartigny, P.; Harris, J.W.; Phillips, D.; Girard, M.; Javoy, M. Subduction-related diamonds?—The evidence for a mantle-derived origin from coupled δC–δN determinations. *Chem. Geol.* **1998**, *147*, 147–159. [CrossRef]

58. Chai, P.; Hou, Z.Q.; Zhang, H.R.; Dong, L.L. Geology, fluid inclusion, and H-O-S-Pb isotope constraints on the mineralization of the Xiejiagou gold deposit in the Jiaodong Peninsula. *Geofluids* **2019**, *2019*, 3726465. [CrossRef]

59. Groves, D.I.; Goldfarb, R.J.; Gebre-Mariam, M.; Hagemann, S.G.; Robert, F. Orogenic gold deposits: A proposed classification in the context of their crustal distribution and relationship to other gold deposit types. *Ore Geol. Rev.* **1998**, *13*, 7–27. [CrossRef]

60. Groves, D.I.; Goldfarb, R.J.; Robert, F.; Hart, C.J.R. Gold deposits in metamorphic belts: Overview of current understanding, outstanding problems, future research, and exploration significance. *Econ. Geol.* **2003**, *98*, 1–29.

61. Zhai, M.G.; Cong, B.L.; Guo, J.H.; Liu, W.J.; Li, Y.G.; Wang, Q.C. Sm-Nd geochronology and petrography of garnet pyroxene granulites in the northern Sulu region of China and their geotectonic implication. *Lithos* **2000**, *52*, 23–33. [CrossRef]

62. Tang, J.; Zheng, Y.F.; Wu, Y.B.; Gong, B.; Zha, X.P.; Liu, X.M. Zircon U-Pb age and geochemical constraints on the tectonic affinity of the Jiaodong terrane in the Suluorogen, China. *Precambrian Res.* **2008**, *161*, 389–418. [CrossRef]

63. Goldfarb, R.J.; Santosh, M. The dilemma of the Jiaodong gold deposits: Are they unique? *Geosci. Front.* **2014**, *5*, 139–153. [CrossRef]

64. Deng, J.; Yang, L.Q.; Groves, D.I.; Zhang, L.; Qiu, K.F.; Wang, Q.F. An integrated mineral system model for the gold deposits of the giant Jiaodong province, eastern China. *Earth-Sci. Rev.* **2020**, *208*, 103274. [CrossRef]

65. Deng, J.; Wang, Q.F.; Liu, X.F.; Zhang, L.; Yang, L.Q.; Yang, L.; Qiu, K.F.; Guo, L.N.; Liang, Y.Y.; Ma, Y. The Formation of the Jiaodong Gold Province. *Acta Geol. Sin.* **2022**, *96*, 1801–1820. [CrossRef]

66. Sack, P.J.; Danyushevsky, L.V.; Large, R.R.; Gilbert, S.; Gregory, D. Sedimentary pyrite as a gold-source in sediment-hosted gold occurrences in the Selwyn basin area, eastern Yukon. *Yukon Explor. Geol.* **2014**, *2013*, 195–220.

67. Augustin, J.; Gaboury, D. Multi-stage and multi-sourced fluid and gold in the formation of orogenic gold deposits in the world class Mana district of Burkina Faso-Revealed by LA-ICP-MS analysis of pyrites and arsenopyrites. *Ore Geol. Rev.* **2019**, *104*, 495–521. [CrossRef]

68. Fridovsky, V.Y.; Polufuntikova, L.I.; Kudrin, M.V. Origin of Disseminated Gold-Sulfide Mineralization from Proximal Alteration in Orogenic Gold Deposits in the Central Sector of the Yana–Kolyma Metallogenic Belt, NE Russia. *Minerals* **2023**, *13*, 394. [CrossRef]

69. Taylor, H.P. The application of oxygen and hydrogen isotope studies to problems of hydrothermal alteration and ore deposition. *Econ. Geol.* **1974**, *69*, 843–883. [CrossRef]

70. Craig, H. Isotopic variations in meteoric waters. *Science* **1961**, *133*, 1702–1704. [CrossRef]

71. Barker, S.L.L.; Hickey, K.A.; Cline, J.S.; Dipple, G.M.; Kilburn, M.R.; Vaughan, J.R.; Longo, A.A. Uncloaking invisible gold: Use of nanoSIMS to evaluate gold, trace elements, and sulphur isotopes in pyrite from Carlin-type gold deposits. *Econ. Geol.* **2009**, *104*, 897–904. [CrossRef]

72. Peterson, E.; Mavrogenes, J. Linking high-grade gold mineralization to earthquake-induced fault-valve processes in the Porgera gold deposit, Papua New Guinea. *Geology* **2014**, *42*, 383–386. [CrossRef]

73. Li, L.; Santosh, M.; Li, S.R. The 'Jiaodong type' gold deposits: Characteristics, origin and prospecting. *Ore Geol. Rev.* **2015**, *65*, 589–611. [CrossRef]

74. Chen, Y.M.; Fan, H.R.; Cui, L.; Wang, Z.K.; Sun, Z.F.; Zeng, Q.D.; Ma, F.S.; Wang, J.T.; Liu, Q.; Sun, Z.F.; et al. *The Large-Scale Gold Mineralization in the Northwestern Jiaodong Terrane and Its Metallogenic Model*; Geological Publishing House: Beijing, China, 2016; pp. 1–336. (In Chinese)

75. Sun, W.D.; Ding, X.; Hu, Y.H.; Li, X.H. The golden transformation of the Cretaceous plate subduction in the west Pacific. *Earth Planet. Sci. Lett.* **2007**, *262*, 533–542. [CrossRef]

76. Deng, J.; Wang, C.; Bagas, L.; Carranza, E.J.M.; Lu, Y. Cretaceous-Cenozoic tectonic history of the Jiaojia Fault and gold mineralization in the Jiaodong Peninsula, China: Constraints from zircon U-Pb, illite K-Ar, and apatite fission track thermochronometry. *Miner. Depos.* **2015**, *50*, 987–1006. [CrossRef]

77. Ohmoto, H. Systematics of sulfur and carbon isotopes in hydrothermal ore deposits. *Econ. Geol.* **1972**, *67*, 551–578. [CrossRef]

78. Bryndzia, L.T.; Scott, S.D. The composition of chlorite as a function of sulfur and oxygen fugacity: An experimental study. *Am. J. Sci.* **1987**, *287*, 50–76. [CrossRef]

79. Deditius, A.P.; Reich, M.; Kesler, S.E.; Utsunomiya, S.; Chryssoulis, S.L.; Walshe, J.; Ewing, R.C. The coupled geochemistry of Au and As in pyrite from hydrothermal ore deposits. *Geochim. Cosmochim. Acta* **2014**, *140*, 644–670. [CrossRef]

80. Deng, J.; Wang, J.G.; Wei, Y.G.; Zhang, Z.Q.; Lin, J.Z.; Yan, S.L. Ores and gold- bearing characteristics in Xiejiagou gold deposit, Shandong Province. *J. Earth Sci.-China* **2007**, *32*, 373–380. (In Chinese with English abstract)

81. Ohmoto, H.; Rye, R.O. Isotopes of sulfur and carbon. In *Geochemistry of Hydrothermal Ore Deposits*, 2nd ed.; Bames, H.L., Ed.; John Wiley & Sons: New York, NY, USA, 1979; pp. 509–567.

82. Cai, Y.C.; Fan, H.R.; Santosh, M.; Hu, F.F.; Yang, K.F.; Li, X.H. Decratonic gold mineralization: Evidence from the Shangzhuang gold deposit, eastern North China Craton. *Gondwana Res.* **2018**, *54*, 1–22. [CrossRef]

83. Yuan, Z.Z.; Li, Z.K.; Zhao, X.F.; Sun, H.S.; Qiu, H.N.; Li, J.W. New constraints on the genesis of the giant Dayingezhuang gold (silver) deposit in the Jiaodong district, North China Craton. *Ore Geol. Rev.* **2019**, *112*, 103038. [CrossRef]

84. Yang, M.Z. *The Geochemistry of Wall Rock Alteration Zone of Gold Deposits As Exemplified by Jiaodong Gold Deposits*; Geological Publishing House: Beijing, China, 1998; pp. 109–112. (In Chinese)

85. Li, H.Q.; Liu, J.Q.; Wei, L. *Chronological Study of Fluid Inclusion for Hydrothermal Deposit and Its Geological Applications*; Geological Publishing House: Beijing, China, 1993; pp. 1–126. (In Chinese)

86. Hodkiewicz, P.F.; Groves, D.I.; Davidson, G.J.; Weinberg, R.F.; Hagemann, S.G. Influence of structural setting on sulphur isotopes in Archean orogenic gold deposits, Eastern Goldfields Province, Yilgarn, Western Australia. *Miner. Depos.* **2009**, *44*, 129–150. [CrossRef]

87. Zhang, L.; Chen, H.Y.; Chen, Y.J.; Qin, Y.J.; Liu, C.F.; Zheng, Y.; Jansen, N.H. Geology and fluid evolution of the Wangfeng orogenic-type gold deposit, Western Tian Shan, China. *Ore Geol. Rev.* **2012**, *49*, 85–89. [CrossRef]

88. Gu, X.X.; Zhang, Y.M.; Ge, Z.L.; Chen, W.Z.; Xu, J.C.; Huang, G.; Tao, W. The orogenic Au mineralization syatem and regional tectonic evolution in the Kalamaili area, East Junggar, Xinjiang. *Earth Sci. Front.* **2020**, *27*, 254–275. (In Chinese with English abstract)

89. Xu, J.C.; Gu, X.X.; Zhang, Y.M.; Wang, J.L.; He, G.; Zhou, C.; Liu, R.P. Geology, fluid inclusions, H-O isotope, and hydrothermal zircon U-Pb geochronology of the Daqingshan orogenic gold deposit in Beishan orogenic belt, Xinjiang, NW China. *Miner. Depos.* **2021**, *56*, 325–342. [CrossRef]

90. Yang, L.Q.; Deng, J.; Wang, Z.L.; Zhang, L.; Guo, L.N.; Song, M.C.; Zheng, X.L. Mesozoic Gold Metallogenic System of the Jiaodong Gold Province, Eastern China. *Acta Petrol. Sin.* **2014**, *30*, 2447–2467. (In Chinese with English abstract)

91. Mills, S.E.; Tomkinsa, A.G.; Weinberga, R.F.; Fan, H.R. Implications of pyrite geochemistry for gold mineralisation and remobilisation in the Jiaodong gold district, northeast China. *Ore Geol. Rev.* **2015**, *71*, 150–168. [CrossRef]

92. Shi, Y.C.; Liu, C.C.; Yang, C.H.; Wang, F.; Li, A.M. Distribution relation and genesis of altered and quartz-vein gold deposits in east Shandong. *Shandong Land Resour.* **2005**, *21*, 19–21. (In Chinese with English abstract)